Peeling and sliding of graphene nanoribbons with periodic van der Waals interactions

Zhiming Xue [a,b], Ganbin Chen [a,c], Changguo Wang [b,d,*], Rui Huang [a,*]

[a] Department of Aerospace Engineering and Engineering Mechanics, University of Texas, Austin, TX 78712, USA
[b] Center for Composite Materials, Harbin Institute of Technology, Harbin 150001, China
[c] Department of Modern Mechanics, University of Science and Technology of China, Hefei, Anhui 230026, China
[d] National Key Laboratory of Science and Technology on Advanced Composites in Special Environments, Harbin Institute of Technology, Harbin 150080, China

ARTICLE INFO

ABSTRACT

The peeling and sliding behaviors of graphene nanoribbons (GNRs) atop a graphene substrate are studied by a continuum model and numerical simulations. A periodic potential energy function is used to simulate the van der Waals interactions between the GNRs and the substrate in both the normal and tangential directions, coupling adhesion and friction within the same model. Numerical simulations and associated analyses reveal remarkably rich dynamics in peeling and sliding of GNRs. It is found that the simple 90-degree peeling of a GNR depends primarily on the normal (adhesive) interactions, with negligible sliding or shear interactions. In contrast, peeling with the end fixed in the in-plane directions leads to stick-slip sliding, with a higher peeling force and a critical peeling angle depending on both adhesion and friction. Notably, the stick-slip sliding is facilitated by formation and gliding of strain solitons in GNRs, and different types of strain solitons may form in the zigzag, armchair and chiral GNRs, including tensile, shear and mixed types. Unconstrained sliding is typically accompanied by both lateral and normal displacements, while constraining the displacements in the normal or lateral directions would generally lead to a higher pulling force for sliding. The peak pulling force as a measure of the sliding friction depends on the ribbon width quasi-linearly but becomes nearly independent of the ribbon length for relatively long GNRs ($L >20$ nm). Finally, two cases with coupled peeling and sliding of GNRs are considered, and a simple analysis is proposed to simultaneously determine the adhesion and friction properties of GNRs from measurable quantities in potential experiments.

1. Introduction

At the interfaces between ultrathin two-dimensional (2D) materials, the mechanical interactions such as adhesion and friction are often coupled intimately with deformation of the 2D materials, leading to a wide range of topological structures and novel properties (Dai et al., 2020). Among many 2D materials, graphene nanoribbons (GNRs) have recently emerged as promising candidates for applications in future nanoelectronic devices including flexible thin-film electronics, optoelectronics, and quantum informatics, due to their exceptional and tunable electronic, optical, thermal, and mechanical properties (Ruffieux et al., 2016; Pour et al., 2017; Slota et al., 2018; Saraswat et al., 2021). The interfacial properties of GNRs are critical for their integration and device applications. Kawai

---

* Corresponding authors.
 E-mail addresses: wangcg@hit.edu.cn (C. Wang), ruihuang@mail.utexas.edu (R. Huang).

et al. (2016) investigated the friction behavior of GNRs sliding on gold surfaces and reported superlubricity with ultralow friction forces (~10–100 pN) measured for GNRs with lengths ranging from 3 to 22 nm. They attributed the superlubricity to the exceptional lateral stiffness of graphene combined with the weak interactions between graphene and the substrate, supported by molecular dynamics (MD) simulations and the classic Prandtl-Tomlinson model for atomic-scale friction. This work was followed by Gigli et al. (2017 and 2018) with systematic MD simulations, showing the effects of edge pinning on the sliding friction of GNRs and predicting a transition from smooth sliding to multiple stick-slip regimes. More recently, Gigli et al. (2019a) conducted experiments and MD simulations of peeling GNRs from a gold substrate with an AFM cantilever, identifying two successive regimes characterized by smooth sliding of the adhered part and then stick-slip with intermittent jumps of the tail end. The rich dynamics of peeling and sliding of GNRs on gold and other substrates may be understood as a result of mixed-mode interactions at the interface with both adhesion and friction.

In recent years, much attention has been paid to stacking 2D materials to form a variety of van der Waals (vdW) materials and heterostructures (Geim and Grigorieva, 2015; Liu et al., 2016; Novoselov et al., 2016; Duong et al., 2017). It is well known that the interlayer friction is low in vdW materials, due to the weak and non-specific vdW interactions between atomically smooth crystal planes. Mandelli et al. (2017) performed atomistic simulations of a finite graphene flake sliding on graphene and hexagonal boron nitride (hBN) substrates. They found that the commensurate graphene/graphene interface exhibited stick–slip motion with size-independent friction coefficients. In contrast, the graphene/hBN interface transitioned from stick-slip motion to smooth sliding as the flake size increased, which was attributed to formation of moiré superstructures due to lattice mismatch. Ouyang et al. (2018) conducted nonequilibrium MD simulations and predicted snake-like sliding motion of narrow GNRs atop graphene and hBN substrates, with an unusual dependence of the friction force on the ribbon length. Using a multiscale computational scheme, Kumar et al. (2016) predicted that only 1–2% strain can be transferred between adjacent layers of 2D materials, depending on the strength of the interlayer vdW interactions and the elastic modulus of the individual layers. They showed that, with a periodic interlayer shear potential, stretching bilayer 2D materials led to formation of strain solitons. Experimentally, an interlayer shear strength of ~0.04 MPa was obtained from bilayer graphene bubbles, much lower than the interfacial shear strength (~1.64 MPa) between graphene and a silicon oxide substrate (Wang et al., 2017). It was found that interlayer sliding between 2D layers has a profound effect on the effective bending stiffness of multilayer vdW materials (Wang et al., 2019; Han et al., 2020). Recently developed nanoscale experiments and devices have demonstrated that the mechanical interactions between 2D layers are often coupled tightly with the electronic and optical properties of vdW materials, leading to a number of intriguing phenomena such as tunable moiré superstructures (Yoo et al., 2019; McGilly et al., 2020).

In this work, we study the mechanical interactions between GNRs and a graphene substrate via peeling and sliding. Both adhesion and friction are considered by using a periodic potential energy function for coupled normal and shear interactions. Based on a continuum model and a finite element method, numerical simulations reveal remarkably rich dynamics in peeling and sliding of GNRs. Moreover, we propose potential experiments for characterizing the adhesion and friction properties of GNRs. The remainder of this paper is organized as follows. A continuum model of GNRs with periodic vdW interactions is described in Section 2. A few analytical solutions for peeling and sliding are presented in Section 3. In Section 4, we describe the finite element method for numerical simulations using a user-defined subroutine (UINTER) for the coupled normal and shear interactions. Section 5 presents a series of numerical results, including peeling, constrained and unconstrained sliding, peeling with sliding, and sliding with a lifted end, along with analyses and discussion. We conclude with a summary of main findings in Section 6. In addition, development of a periodic potential energy function for the vdW interactions based on atomistic calculations is presented as an appendix, and additional numerical results are provided in Supplementary Information (SI).

2. A continuum model

This section describes a continuum model for peeling and sliding of GNRs atop a graphene substrate as illustrated in Fig. 1. The GNR is treated as a linearly elastic sheet with the effective elastic properties of monolayer graphene (Lu et al., 2011), while the vdW interactions between the GNR and the substrate is simulated by using a periodic potential energy function; the substrate is assumed to be rigid. The edge effects on the elastic and interfacial properties of the GNRs are ignored for the present study.

2.1. A periodic interlayer potential for van der Waals interactions

Following Kumar et al. (2015 and 2016), we write the interlayer potential energy (per unit area) as a function of the displacement (u_x, u_y, u_z) of the GNR relative to its substrate as:

$$U(u_x, u_y, u_z) = U_0(u_z) + U_1(u_z)f(u_x, \ u_y). \tag{1}$$

The first term on the right-hand side of Eq. (1) describes the dependence of the interaction potential energy on the normal separation (u_z) of the GNR in a commensurate AB stacking ($u_x = u_y = 0$) and takes the form (Zhang and Tadmor, 2017)

$$U_0(u_z) = \frac{\varepsilon_0}{A_0} \left[-\frac{5}{3} \left(\frac{z_0}{z_0 + u_z} \right)^4 + \frac{2}{3} \left(\frac{z_0}{z_0 + u_z} \right)^{10} \right], \tag{2}$$

where $z_0 = 0.334$ nm (the equilibrium separation), $\varepsilon_0 = 0.0411$ eV, $A_0 = \frac{3\sqrt{3}}{4}a^2$ with $a = 0.142$ nm (the C—C bond length in graphene). The adhesion energy for the commensurate AB stacking is then: $\Gamma_0 = \frac{\varepsilon_0}{A_0} = 0.25$ J/m², close to measurements (Koren et al., 2015;
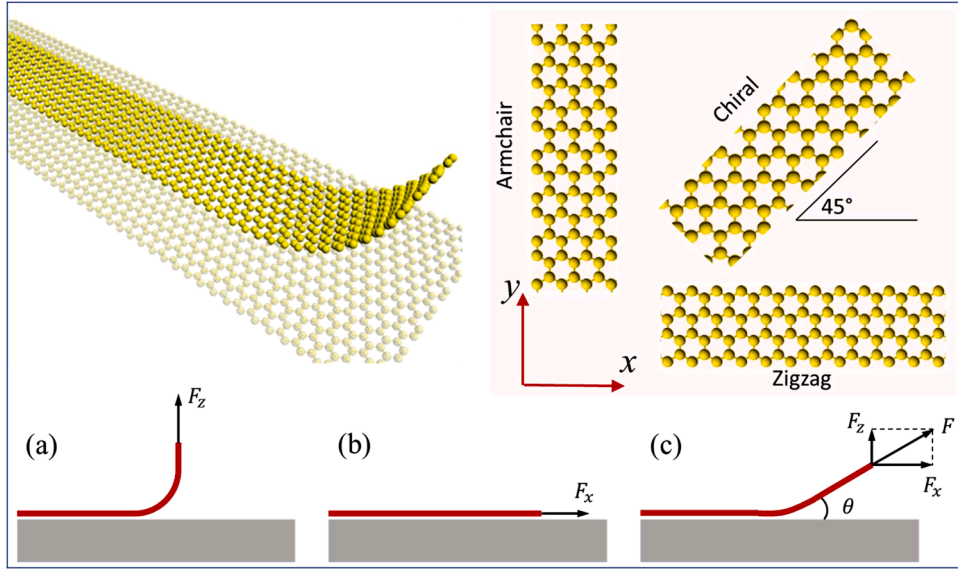
Fig. 1. Top: schematic illustration of a monolayer graphene nanoribbon on a graphene substrate and three GNR orientations. Bottom: side views of (a) peeling, (b) sliding, and (c) coupled peeling and sliding of a GNR.

Sanchez et al., 2018) and DFT calculations (Duong et al., 2017).

The second term on the right-hand side of Eq. (1) describes the periodic corrugation of the potential energy with respect to the in-plane displacements, u_x and u_y, from the commensurate stacking with

$$f\left(u_x,\ u_y\right) = \frac{3}{2} + \cos\left(G_1\left(u_y - a\right)\right) + 2\cos\left(\frac{G_1\left(u_y - a\right)}{2}\right)\cos\left(\frac{\sqrt{3}G_1 u_x}{2}\right), \tag{3}$$

and

$$U_1\left(u_z\right) = \frac{\varepsilon_1}{A_0}\left[-\left(\frac{z_0}{z_0 + u_z}\right)^4 + \beta\left(\frac{z_0}{z_0 + u_z}\right)^{10}\right], \tag{4}$$

where $G_1 = \frac{4\pi}{3a}$, $\varepsilon_1 = 1.33 \times 10^{-4}$ eV, and $\beta = 28.7$; the values of ε_1 and β were obtained by fitting to atomistic calculations (see Appendix for details). Here, the in-plane coordinates are set up such that the x-axis is parallel to a zigzag direction of the graphene lattice and the y-axis is parallel to an armchair direction (see Fig.1). We note that the interlayer potential energy as described here assumes a commensurate stacking for the GNR before peeling or sliding.

The normal and shear tractions at the interface can be obtained from the periodic interlayer potential function as:

$$\sigma = \frac{\partial U}{\partial u_z} = \sigma_0(u_z) + \sigma_1(u_z)f\left(u_x,\ u_y\right), \tag{5}$$

$$\tau_x = \frac{\partial U}{\partial u_x} = -\sqrt{3}G_1 U_1(u_z)\sin\left(\frac{\sqrt{3}}{2}G_1 u_x\right)\cos\left(\frac{G_1\left(u_y - a\right)}{2}\right), \tag{6}$$

$$\tau_y = \frac{\partial U}{\partial u_y} = -G_1 U_1(u_z)\left[\sin\left(G_1\left(u_y - a\right)\right) + \sin\left(\frac{G_1\left(u_y - a\right)}{2}\right)\cos\left(\frac{\sqrt{3}G_1 u_x}{2}\right)\right], \tag{7}$$

where

$$\sigma_0(u_z) = \frac{20\Gamma_0}{3z_0}\left[\left(\frac{z_0}{z_0 + u_z}\right)^5 - \left(\frac{z_0}{z_0 + u_z}\right)^{11}\right], \tag{8}$$

$$\sigma_1(u_z) = \frac{\varepsilon_1}{A_0 z_0}\left[4\left(\frac{z_0}{z_0 + u_z}\right)^5 - 10\beta\left(\frac{z_0}{z_0 + u_z}\right)^{11}\right]. \tag{9}$$
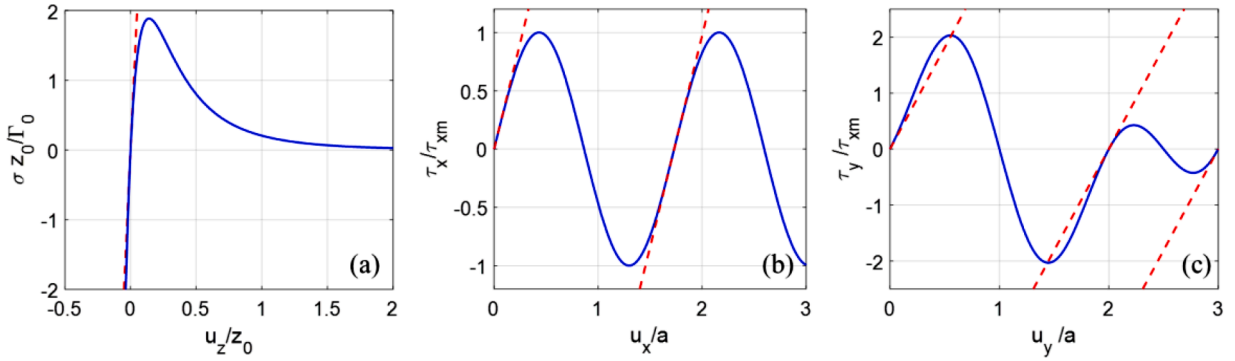
Fig. 2. (a) Normal traction (normalized by Γ_0/z_0) as a function of the normal separation (normalized by z_0); (b-c) Shear traction (normalized by τ_{xm}) as a function of the sliding displacement (normalized by a) in the x (zigzag) and y (armchair) directions, respectively. The dashed lines show the linearized traction-displacement relations.

2.2. A continuum model for peeling

The peeling model consists of a GNR (Fig. 1a) of length L and width b ($b \ll L$), initially lying flat on the substrate to which it adheres with a potential energy per unit area, $U(0,0,0) = -\Gamma_0$. The GNR is then peeled off by lifting one end with a force in the normal direction (F_z). The normal displacement of the GNR in general could be large, with nonlinear effects due to the interlayer traction-separation relation (Fig. 2a) and the kinematics of bending deformation, while the in-plane strain of the GNR is relatively small so that the GNR remains linearly elastic. At the initial stage of peeling, when the normal displacement (u_z) is relatively small (compared to z_0), the mechanical equilibrium requires that (Timoshenko and Woinowsky-Krieger, 1987)

$$D\frac{d^4u_z}{dx^4} = -\sigma(u_z), \tag{10}$$

where D is the bending modulus of graphene ($\sim$1.5 eV) and σ is the normal traction as given in Eq. (5). Note that the tangential components of the traction are negligible in this case since the applied force has zero tangential components (i.e., 90-degree peeling). As a result, we assume that $u_x = u_y = 0$ and hence $\sigma(u_z) = \sigma_0(u_z)$ as shown in Fig. 2a. These assumptions will be relaxed in numerical simulations in Section 5.

2.3. A continuum model for sliding

Fig. 1b illustrates sliding of a GNR in the x direction, subject to a pulling force (F_x) at one end. In general, the sliding direction depends on the edge orientation of the GNR (e.g., zigzag and armchair as illustrated in Fig. 1). Consider sliding of a zigzag GNR in the x direction first. Assuming the GNR to be linearly elastic, the mechanical equilibrium requires that

$$Et\frac{d^2u_x}{dx^2} = \tau_x(u_x), \tag{11}$$

where Et is the 2D Young's modulus of graphene ($\sim$345 N/m) with an effective thickness t, τ_x is the shear traction at the interface as given in Eq. (6), and u_x is the axial displacement of the GNR. Here we assume one-dimensional (1D) sliding with $u_z = u_y = 0$ so that τ_x depends on u_x only (Fig. 2b); this assumption will be relaxed in numerical simulations. Similarly, for 1D sliding in the y direction, we assume $u_z = u_x = 0$ so that τ_y depends on u_y only (Fig. 2c). It turns out that the displacement is generally 3D during unconstrained sliding as discussed in Section 5.2.

3. Analytical solutions

3.1. Peeling

For a small peeling displacement ($u_z \ll z_0$), the normal traction in Eq. (5) can be linearized (see Fig. 2a) as:

$$\sigma(u_z) \approx \frac{40\Gamma_0}{z_0^2}u_z = k_z u_z, \tag{12}$$

where $k_z = \frac{40\Gamma_0}{z_0^2}$ is the initial stiffness of the normal interaction. With Eq. (12) for the normal traction, Eq. (10) can be solved analytically as

$$u_z(x) = \left(A_1 \sin\frac{x}{\lambda_z} + A_2\cos\frac{x}{\lambda_z} \right)\cosh\frac{x}{\lambda_z} + \left(A_3\sin\frac{x}{\lambda_z} + A_4\cos\frac{x}{\lambda_z} \right)\sinh\frac{x}{\lambda_z},$$

(13)

where $\lambda_z = (4D/k_z)^{1/4}$ is a characteristic length scale (~ 0.32 nm).

Apply the boundary conditions: $\frac{d^2 u_z}{dx^2}\big|_{x=0,L} = 0$ and $u_z|_{x=L} = \delta_z$ (end separation), along with the conditions of force and moment balance, i.e., $F_z = b \int_0^L \sigma dx$ and $F_z L = b\int_0^L \sigma x dx$, which combine to yield: $\int_0^L \sigma(L-x)dx = 0$. The coefficients in Eq. (13) are obtained as:

$$A_1 = A_4 = \delta_z \frac{2\sinh\left(\frac{L}{\lambda_z}\right)\sin\left(\frac{L}{\lambda_z}\right)}{\sinh\left(\frac{2L}{\lambda_z}\right) - \sin\left(\frac{2L}{\lambda_z}\right)}, \quad A_2 = \delta_z \frac{\sec\left(\frac{L}{\lambda_z}\right)\mathrm{sech}\left(\frac{L}{\lambda_z}\right)\left(\tan\left(\frac{L}{\lambda_z}\right) - \tanh\left(\frac{L}{\lambda_z}\right)\right)}{\mathrm{sech}^2\left(\frac{L}{\lambda_z}\right)\tan\left(\frac{L}{\lambda_z}\right) - \sec^2\left(\frac{L}{\lambda_z}\right)\tanh\left(\frac{L}{\lambda_z}\right)}, \text{ and } A_3 = 0. \text{ The reaction force at the peeling end is then}$$

obtained as: $F_z = bD\frac{d^3 u_z}{dx^3}\big|_{x=L}$ (or equivalently, $F_z = b\int_0^L \sigma dx$), which is linearly proportional to the end separation δ_z with an effective peeling stiffness:

$$K_z = \frac{F_z}{\delta_z} = \frac{1}{2}k_z\lambda_z b\left(\frac{\cosh(2L/\lambda_z) + \cos(2L/\lambda_z) - 2}{\sinh(2L/\lambda_z) - \sin(2L/\lambda_z)} \right).$$

(14)

For a relatively long GNR ($L \gg \lambda_z$), we obtain a constant peeling stiffness: $K_z^\infty = \frac{1}{2}k_z\lambda_z b$, which is independent of the GNR length but linearly proportional to the GNR width. Thus, the effective peeling stiffness (K_z^∞) can be directly related to the interlayer stiffness (k_z) for the normal interactions.

Moreover, for a relatively long GNR ($L \gg \lambda_z$), a steady-state solution for peeling can be obtained from an energetic consideration (Rivlin, 1944), which predicts a constant peeling force at large separation ($\delta_z \gg z_0$):

$$F_z^{SS} = \Gamma_0 b.$$

(15)

Thus, the steady-state peeling force can be directly related to the adhesion energy. We note that Eq. (15) is obtained by assuming the GNR to be inextensible, which is reasonable in the present case because the in-plane stiffness of monolayer graphene ($Et = 345$ N/m) is much larger than the adhesion energy ($\Gamma_0 = 0.25$ N/m) and thus the effect of elastic strain energy in the GNR on the steady-state peeling force (Kendell, 1975) is negligible.

3.2. One-dimensional sliding

Consider one-dimensional (1D) sliding in the x direction with $u_y = u_z = 0$. By Eq. (6), we obtain the shear traction:

$$\tau_x(u_x) = \frac{\sqrt{3}}{2}U_{1e}G_1\sin\left(\frac{\sqrt{3}}{2}G_1 u_x \right) = \tau_{xm}\sin\left(\frac{\sqrt{3}}{2}G_1 u_x \right),$$

(16)

where $U_{1e} = U_1(0) = (\beta - 1)\varepsilon_1/A_0$ and $\tau_{xm} = \frac{\sqrt{3}}{2}U_{1e}G_1 = (\beta - 1)\frac{8\pi\varepsilon_1}{9a^3}$ (i.e., shear strength of the interface). Substituting Eq. (16) into Eq. (11), we obtain

$$Et\frac{d^2 u_x}{dx^2} = \tau_{xm}\sin\left(\frac{\sqrt{3}}{2}G_1 u_x \right),$$

(17)

which is a static form of the sine-Gordon equation as in the 1D Frenkel-Kontorova model (Braun and Kivshar, 2004). It is known that the sine-Gordon equation admits many possible solutions, including homogeneous solutions with a constant displacement at discrete levels (e.g., $G_1 u_x = 2n\pi/\sqrt{3}$ with $n = 0,1,2,\ldots$) and inhomogeneous solutions with strain solitons.

Let $\varepsilon_x = \frac{du_x}{dx}$ as the axial strain of the GNR, and re-write Eq. (17) as

$$Et\varepsilon_x\frac{d\varepsilon_x}{du_x} = \tau_{xm}\sin\left(\frac{\sqrt{3}}{2}G_1 u_x \right).$$

(18)

For an infinitely long GNR ($L \to \infty$), Eq. (18) can be integrated to yield[1]

$$\varepsilon_x = \sqrt{\frac{4\tau_{xm}}{\sqrt{3}G_1 Et}\left[1 - \cos\left(\frac{\sqrt{3}}{2}G_1 u_x \right) \right]},$$

(19)

where the strain has a maximum magnitude when $G_1 u_x = 2n\pi/\sqrt{3}$ (with $n = 1,3,\ldots$):

---

[1] This is possible only for an infinitely long ribbon with zero displacement and zero strain at the tail end.

$$\varepsilon_{xm} = \sqrt{\frac{8\tau_{xm}}{\sqrt{3}G_1 Et}}. \tag{20}$$

For the present model, we obtain $\varepsilon_{xm} = \frac{4}{3^{3/4}} \sqrt{\frac{(\beta-1)\varepsilon_1}{Eta^2}} = 0.0162$ for 1D sliding of the GNR. Thus, the strain remains relatively small during sliding, consistent with the assumption of linear elasticity for the GNR. We note a similar but different prediction of the maximum strain (~ 0.011) by Kumar et al. (2016), where a linear approximation was used to obtain an analytical solution.

The pulling force (F_x) at the front end of the GNR is a function of the pulling displacement (δ_x). Following Eq. (19), we obtain

$$F_x = Etb\varepsilon_x = b\sqrt{\frac{4\tau_{xm}Et}{\sqrt{3}G_1}\left[1 - \cos\left(\frac{\sqrt{3}}{2}G_1\delta_x\right)\right]}, \tag{21}$$

which predicts a maximum force (~ 5.6 N/m, per unit width of the GNR)

$$F_x^{max} = \frac{4b}{3^{3/4}a}\sqrt{(\beta-1)Et\varepsilon_1}. \tag{22}$$

For small values of u_x ($\ll a$), the shear traction in Eq. (16) can be linearized (Fig. 2b) as:

$$\tau_x \approx \frac{\sqrt{3}}{2}\tau_{xm}G_1 u_x = k_x u_x, \tag{23}$$

where $k_x = \frac{\sqrt{3}}{2}\tau_{xm}G_1$ is the initial stiffness of the shear interactions.

Inserting Eq. (23) into Eq. (11), we obtain:

$$\frac{d^2 u_x}{dx^2} = \frac{u_x}{\lambda_x^2}, \tag{24}$$

where $\lambda_x = \sqrt{\frac{Et}{k_x}}$ is a characteristic length scale for the shear interactions (~ 4.85 nm). Note that $\lambda_x \gg \lambda_z$.

Solving Eq. (24), we obtain:

$$u_x(x) = B_1 \cosh\left(\frac{x}{\lambda_x}\right) + B_2 \sinh\left(\frac{x}{\lambda_x}\right). \tag{25}$$

To determine the coefficients B_1 and B_2, we apply the boundary conditions. With $\frac{du_x}{dx} = 0$ at $x = 0$ (the tail end), we obtain $B_2 = 0$. At the other end ($x = L$), we have $\frac{du_x}{dx} = \frac{F_x}{Etb}$, with which we obtain $B_1 = \frac{F_x}{Etb}\frac{\lambda_x}{\sinh(L/\lambda_x)}$. Therefore, the sliding displacement of the GNR is:

$$u_x(x) = \frac{F_x\lambda_x}{Etb}\frac{\cosh(x/\lambda_x)}{\sinh(L/\lambda_x)}. \tag{26}$$

The pulling displacement at the front end is: $\delta_x = u_x(x = L)$, which is linearly proportional to the pulling force with an effective sliding stiffness:

$$K_x = \frac{F_x}{\delta_x} = \frac{Etb}{\lambda_x}\tanh\left(\frac{L}{\lambda_x}\right). \tag{27}$$

For a relatively long GNR ($L \gg \lambda_x$), the sliding stiffness is independent of the length: $K_x^\infty = \frac{Etb}{\lambda_x} = b\sqrt{Etk_x}$, which can be related to the stiffness (k_x) and strength ($\tau_{xm} = \frac{2k_x}{\sqrt{3}G_1}$) of the shear interactions.

We note that sliding of GNRs in general may depend on the GNR orientation and the sliding direction. For 1D sliding of an armchair GNR in the y-direction, the primary shear traction is obtained from Eq. (7) as:

$$\tau_y(u_y) = -U_{1e}G_1\left[\sin(G_1(u_y - a)) + \sin\left(\frac{G_1(u_y - a)}{2}\right)\right], \tag{28}$$

which has a period of $3a$ and a maximum stress, $\tau_{ym} = 1.76U_{1e}G_1$ (about twice of the shear strength in the x-direction) as shown in Fig. 2c. Then, by Eq. (11), we obtain

$$Et\varepsilon_y\frac{d\varepsilon_y}{du_y} = -U_{1e}G_1\left[\sin(G_1(u_y - a)) + \sin\left(\frac{G_1(u_y - a)}{2}\right)\right]. \tag{29}$$

Integrating Eq. (29) yields

$$\varepsilon_y = \sqrt{\frac{2U_{1e}}{Et}\left[\cos(G_1(u_y - a)) + 2\cos\left(\frac{G_1(u_y - a)}{2}\right) + \frac{3}{2}\right]^{1/2}}. \tag{30}$$

Here, the strain is zero when $u_y = 3na$ or $(3n-1)a$ (for $n = 0, 1, 2, ...$) and has a maximum at $\varepsilon_{ym} = \sqrt{\frac{9U_{1e}}{Et}} = 0.024$ when u_y

$= (3n+1)a \, (n = 0,1,2,\ldots)$. In addition, the strain has a secondary (local) maximum at $\frac{1}{3}\varepsilon_{ym} = 0.008$ when $u_y = (3n-1/2)a$ (for $n = 0,1, 2,\ldots$).

Following Eq. (30), we obtain the pulling force (F_y) at the front end of the GNR as a function of the pulling displacement (δ_y):

$$F_y = Etb\varepsilon_y = b\sqrt{2EtU_{1e}}\left[\cos\left(G_1\left(\delta_y - a\right)\right) + 2\cos\left(\frac{G_1\left(\delta_y - a\right)}{2}\right) + \frac{3}{2}\right]^{1/2}, \tag{31}$$

which predicts a maximum force

$$F_y^{max} = \frac{6b}{3^{3/4}a}\sqrt{(\beta - 1)Et\varepsilon_1}. \tag{32}$$

A comparison between Eqs. (32) and (22) suggests that the maximum pulling force for 1D sliding of an armchair GNR in the y direction is exactly 50% higher than that for a zigzag GNR sliding in the x direction, although the interlayer shear strength is about twice ($\tau_{ym} \approx 2\tau_{xm}$). Interestingly, the secondary peak force for sliding in the y direction is 1/3 of the maximum force in Eq. (32) and one half of the maximum force in Eq. (22) for sliding in the x direction. Notably, the maximum pulling forces as predicted by Eq. (22) and (32) are independent of the length of the GNRs and linearly proportional to the GNR width. This suggests that the critical force for sliding friction of a GNR is not directly related to the area of GNR or the contact area between the GNR and the substrate, in sharp contrast with uniform sliding of rigid graphene flakes (Verhoeven et al., 2004; Guo et al., 2007). Despite the fairly small maximum strains ($\sim 1.6\%$ and 2.4%) in the GNRs, the effect of elastic deformation on sliding friction cannot be neglected in general. As we show in Section 5.2, the assumption of a rigid flake can be justified only for very short GNRs ($L \le 5$ nm).

Linearizing Eq. (28) for small sliding displacements ($u_y \ll z_0$), we obtain

$$\tau_y \approx \frac{3}{4}U_{1e}G_1^2 u_y = k_y u_y, \tag{33}$$

where $k_y = \frac{3}{4}U_{1e}G_1^2$. It is found that $k_y \equiv k_x$. The initial stiffness of the shear interactions is isotropic for graphene, dictated by the hexagonal symmetry of the graphene lattice. However, the edge effects (if considered) may lead to an anisotropic sliding stiffness for GNRs as the elastic properties of the GNRs become anisotropic (Lu et al., 2011) and the vdW interactions may depend on the specific edge structures (Jia et al., 2009; Lu and Huang, 2010; Acik and Chabal, 2011). Moreover, even with the edge effects ignored, it is found that the sliding behavior becomes anisotropic in the nonlinear regime, as predicted by Eqs. (21) and (31) for the zigzag and armchair GNRs, respectively, and by numerical simulations in Section 5.2.

We note that the assumptions in the 1D sliding model includes constrained lateral displacement ($u_y = 0$ or $u_x = 0$) and zero normal displacement ($u_z = 0$). These assumptions will be relaxed in the finite element model (Section 4), and the numerical results (Section 5) will be compared to the analytical predictions.

4. Finite element method

The periodic interlayer potential energy function as given in Eq. (1) is highly nonlinear. As a result, the peeling and sliding behaviors of GNRs are expected to be nonlinear in general. To simulate the nonlinear peeling and sliding of GNRs, we employ a finite element method (FEM) using the commercial software ABAQUS. The GNR is modeled by shell elements (S4R, element size ~ 0.15–0.5 nm), with linearly elastic properties (Akinwande et al., 2017): 2D Young's modulus $Et = 345$ N/m, Poisson's ratio $\nu = 0.16$, and a bending modulus $D = 1.5$ eV. The effective thickness for the shell element can be obtained as: $t = \sqrt{\frac{12D}{Et}(1 - \nu^2)} = 0.09$ nm, and the effective Young's modulus is then: $E = \frac{345 \, (\text{N/m})}{0.09 \, (\text{nm})} = 3.83$ (TPa). The effective thickness and Young's modulus have no physical meaning, but together they yield the equivalent 2D Young's modulus (Et) and the bending modulus (D) for a monolayer graphene. The substrate is modeled as a rigid body in this study, and the periodic interlayer potential energy function is implemented as a user-defined subroutine (UINTER) for the vdW interactions between the GNR and the substrate.

We conduct dynamic implicit simulations in ABAQUS to mitigate numerical instability (due to stick-slip or snap transitions). The mass density of bulk graphite is 2260 kg/m³. The mass per unit area of monolayer graphene is then: $2260(\text{kg}/\text{m}^3) \times 0.334(\text{nm}) = 7.56 \times 10^{-7} \, (\text{kg}/\text{m}^2)$. For the shell element with the effective thickness ($t = 0.09$ nm), the effective mass density of graphene is obtained as: $\frac{7.56 \times 10^{-7} (\text{kg/m}^2)}{0.09(\text{nm})} = 8387$ (kg/m³). Again, the effective mass density has no physical meaning by itself. Here, for the purpose of numerical stabilization, a mass scaling factor of 1000 is used for quasistatic simulations, where the resulting kinetic energy remains negligible. In addition, to minimize the rate effect, we apply sufficiently small rates for the peeling and sliding displacements so that the results are rate-independent. To further mitigate the dynamic effect, we may hold the applied displacement unchanged at the points of stick-slip and continue loading after the oscillations disappear (due to numerical damping).

5. Numerical results and discussion

5.1. Peeling

We first consider the case of simple peeling, where a peeling force is applied in the normal direction (Fig. 1a) and the lifted end of
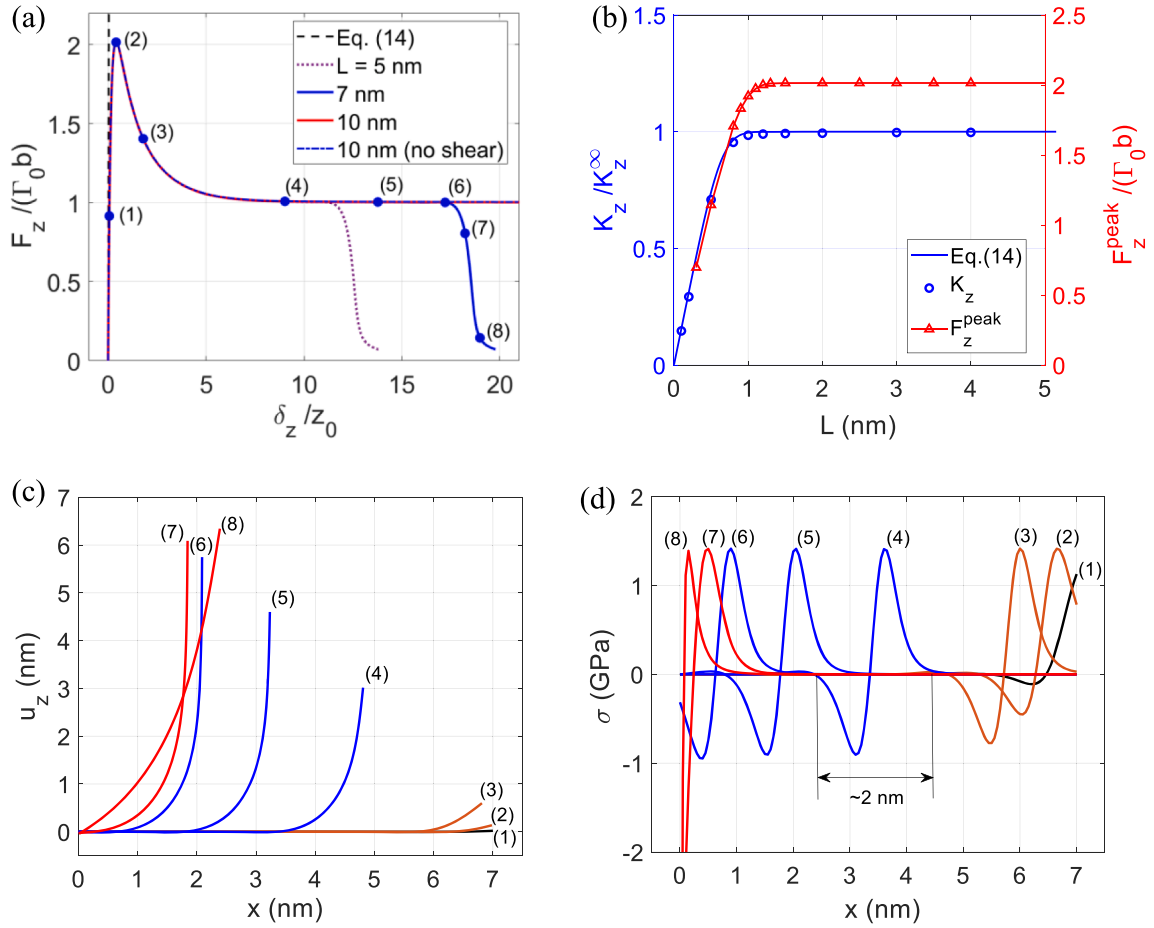
Fig. 3. (a) Normalized peeling force as a function of the end separation of the GNRs with different lengths (ribbon width $b = 1$ nm). (b) Normalized initial peeling stiffness (left axis) and the peak peeling force (right axis) versus the ribbon length. (c) Deflection profiles of a GNR ($L = 7$nm) and (d) the interlayer normal tractions at different end separations, corresponding to the points (1) to (8) in (a).

the GNR is free to move in the x-y plane. This is similar to the classical 90-degree peeling tests (Rivlin, 1944; Kendell, 1975). Fig. 3a shows the peeling force as a function of the end separation for three GNRs with different lengths. The peeling force first increases linearly and then reaches a peak value (F_z^{peak}), followed by a gradual decrease, approaching a plateau (F_z^{SS}) for steady-state peeling of a relatively long ribbon ($L > 5$ nm). Eventually, the peeling force drops from the plateau and approaches zero for a complete peel-off. The initial peeling stiffness (K_z), the peak peeling force ($F_z^{peak} \sim 2F_z^{SS}$), and the steady-state peeling force ($F_z^{SS} = \Gamma_0 b$) are independent of the ribbon length for $L > 5$ nm. As shown in Fig. 3b, the peeling stiffness remains a constant even for a very short ribbon until the ribbon length is less than ~ 1 nm, as predicted by Eq. (14) with a very short characteristic length ($\lambda_z \sim 0.32$ nm) for the normal (adhesive) interactions. Similarly, the peak force remains a constant (proportional to the ribbon width, $\sim 2\Gamma_0 b$) for $L > 1$ nm but becomes smaller for very short ribbons ($L < 1$ nm).

Fig. 3c shows the deflection profiles of one GNR ($L = 7$ nm) at different end separations, corresponding to the points (1) to (8) in Fig. 3a. It is found that the peak force is reached when the end separation $\delta_z = 0.41z_0 = 0.137$ nm, which is about 3 times of the normal separation for the maximum normal traction in Fig. 2a. At this point, the normal traction distribution along the interface (Fig. 3d) shows a positive and a negative peak near the peeling end of the GNR. The negative traction (compressive or repulsion) develops as a result of bending of the GNR, which competes with the positive traction (tensile or attraction) to set up the peak force. Further increasing the end separation leads to a lower peeling force as the negative traction increases faster than the positive traction. When the end separation reaches about $9z_0$ (~ 3 nm), the peeling force reaches the steady-state value as predicted by Eq. (15), $F_z^{SS} = \Gamma_0 b$. At this point, the normal traction is zero at both ends of the GNR, but varies from positive to negative within a small interaction zone (~ 2 nm). As the end separation increases further, the interaction zone translates toward the other end of the GNR, while the traction distribution within the interaction zone remains the same so that the peeling force maintains at the steady-state value until the interaction zone reaches the tail end of the GNR. Subsequently, the interaction zone size decreases and the peeling force drops towards zero. While the same steady-state peeling force is reached for GNRs of different lengths ($L = 5$ nm or longer), the dropping of the
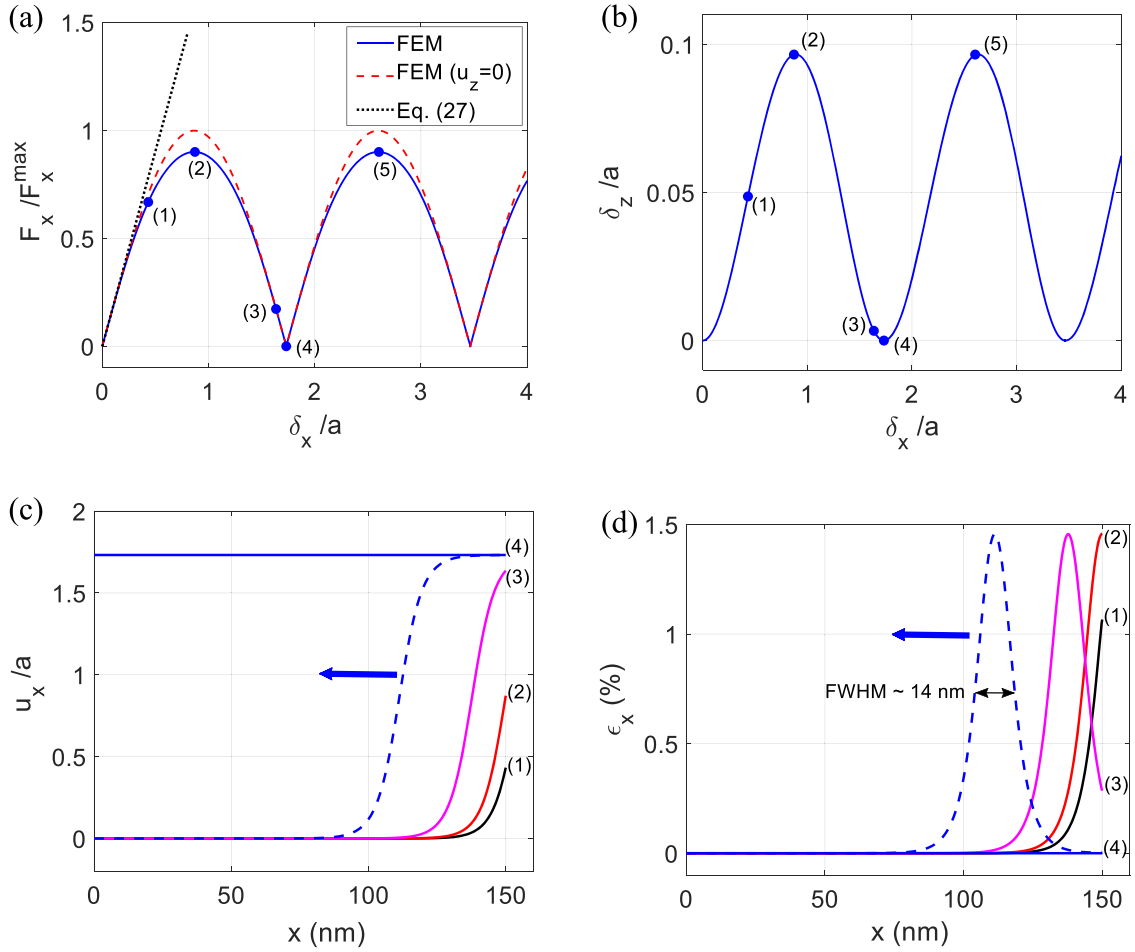
Fig. 4. Simulation of 1D sliding of a zigzag GNR ($L = 150$ nm and $b = 1$ nm) in the x direction with constrained lateral displacement. (a) Normalized pulling force, and (b) normal displacement of the pulling end as a function of the pulling displacement, where the force is normalized by the predicted maximum force in Eq. (22). (c) Evolution of the sliding displacement, and (d) the corresponding axial strain distributions. The dashed lines in (c) and (d) show the displacement and strain of a gliding strain soliton.

peeling force occurs at a smaller end separation for a shorter GNR. For GNRs shorter than 5 nm, the peeling force drops continuously after the peak (see Fig. S1 in SI), with no steady state.

The peeling behavior of a relatively long GNR ($L > 5$ nm) as shown in Fig. 3 is thus characterized by three key parameters: the initial stiffness (K_z), the peak force (F_z^{peak}), and the steady-state force (F_z^{SS}). The peeling behavior largely depends on the first term of Eq. (5) for the normal interactions, whereas the second term of Eq. (5) and the shear interactions are negligible, because the in-plane displacements (u_x and u_y) are nearly zero within the interaction zone. Since no external force is applied in the x or y direction (Fig. 1a), there is zero net force pulling the flat part of the GNR in the x or y direction, and thus the adhered part of the GNR remains in the commensurate AB stacking on the substrate with no sliding during the peeling process. As shown in Fig. 3a, the FEM results remain essentially the same when the shear interactions are turned off in the UINTER implementation. It is also noted that the peeling behavior is independent of the GNR orientation by the present model, although the edge effect (not considered here) could potentially introduce an orientation dependence for both the elastic properties of the GNRs (Lu et al., 2011) and the interlayer forces (along the edges). Without considering the edge effect, the peeling force is linearly proportional to the ribbon width.

As in the classical peeling tests (Rivlin, 1944), measurement of the steady-state peeling force (F_z^{SS}) can determine the adhesion energy as $\Gamma_0 = F_z^{SS}/b$. In addition, measurement of the initial stiffness (K_z) may be used to determine the equilibrium separation for the vdW interactions: $z_0 = \sqrt{\frac{40\Gamma_0}{k_z}}$ with $k_z = \left(\frac{4K_z^4}{Db^4}\right)^{1/3}$ by Eq. (14). Alternatively, measurements of the peak force ($F_z^{peak} \sim 2\Gamma_0 b$) and the corresponding end separation ($\delta_z \sim 0.41 z_0$) may also be used to determine the adhesion energy and the equilibrium separation.
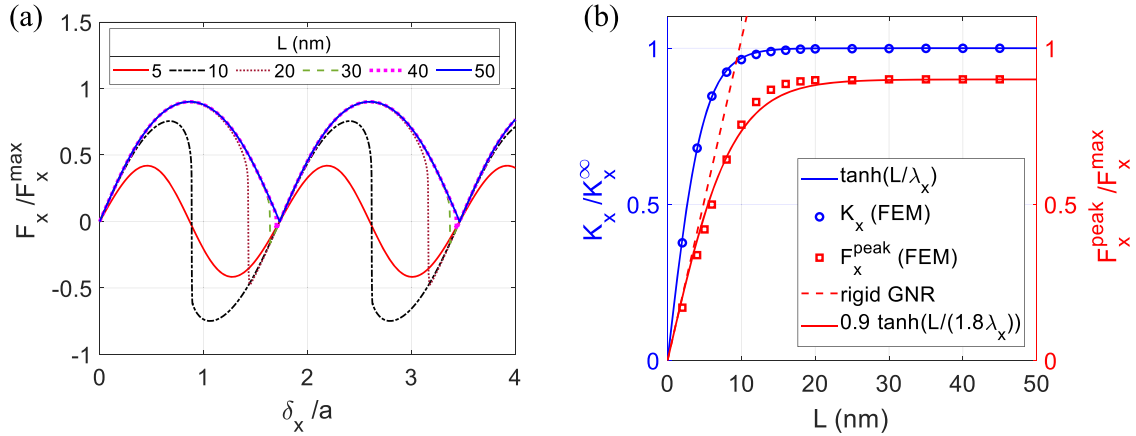
Fig. 5. Effects of the ribbon length on 1D sliding of zigzag GNRs in the x direction with constrained lateral displacement. (a) Normalized pulling force as a function of the pulling displacement with different GNR lengths. (b) Normalized initial sliding stiffness (left axis) and the peak force (right axis) versus the GNR length.

5.2. Sliding

5.2.1. Constrained 1D sliding

For sliding we first consider 1D sliding of a zigzag GNR along the x direction with the lateral displacement constrained ($u_y = 0$). Fig. 4a shows the pulling force (F_x) at the right end as a function of the pulling displacement (δ_x) for a relatively long GNR ($L = 150$ nm). The pulling force first increases linearly, following the analytical solution in Eq. (27) with an initial stiffness ($K_x = b\sqrt{Etk_x}$). The numerical result starts deviating from the linear solution when the pulling displacement is greater than a fraction of the bond length a, with a peak force at $\delta_x = \sqrt{3}a/2$ followed by a periodic variation. The variation period is $\sqrt{3}a$, corresponding to the structural periodicity along the zigzag direction of the graphene lattice (or the edge of the zigzag GNR). This behavior is in sharp contrast with what may be expected from a uniform sliding of a rigid flake (Guo et al., 2007), in which case the shear traction would be uniformly distributed along the interface and the peak pulling force (at $\delta_x = \sqrt{3}a/4$) would be much larger. Moreover, with uniform sliding ($u_x = \delta_x$), the shear traction by Eq. (16) has the same period but becomes negative when $\sqrt{3}/2 < \delta_x/a < \sqrt{3}$ (see Fig. 2b). Evidently, the elastic deformation of the GNR has a significant effect on the sliding behavior. Furthermore, it is found that the in-plane sliding of the GNR is accompanied by a periodic normal displacement (u_z) as shown in Fig. 4b. Although the magnitude of the normal displacement is small ($\sim 0.1a$), it has an appreciable effect on the peak pulling force. As shown in Fig. 4a, if the normal displacement of the GNR is suppressed by setting $u_z \equiv 0$, the peak pulling force would be higher by about 10%. In this case, the numerical results are in close agreement with the prediction by Eq. (21) with the predicted maximum force in Eq. (22). Evidently, the peak force is reduced by allowing the normal displacement, which may be interpreted as reduced friction.

Fig. 4c shows the sliding displacement along the GNR at different pulling displacements, corresponding to the points (1) to (4) in Fig. 4a. Unlike uniform sliding, the displacement initially is localized near the pulling end within a sliding zone while the rest of the GNR does not slide at all. The localized displacement in the sliding zone is accommodated by an axial strain of the GNR (Fig. 4d). As the pulling displacement increases, the sliding zone expands and the strain at the pulling end reaches a peak (point 2) and then drops (point 3). The peak strain is about 1.5%, slightly lower than the prediction by Eq. (20) due to the presence of normal displacement. When the pulling displacement reaches a critical value ($\sqrt{3}a$), a strain soliton forms and glides toward the other end of the GNR, while the pulling force drops to zero (point 4). Without further pulling at the end, the strain soliton glides all the way with no resistance[2] and vanishes at the tail end of the GNR, after which the strain becomes zero everywhere in the GNR and the entire GNR has slid by a constant displacement ($u_x = \sqrt{3}a$). The same sliding process repeats as the pulling continues. We note that such a sliding behavior is reminiscent of the stick-slip behavior of atomic friction (Mandelli et al., 2017; Gao, 2010), and the gliding of strain soliton resembles dislocation gliding in crystals during plastic deformation. In particular, most part of the GNR remains "stuck" ($u_x = 0$) until the pulling displacement reaches the critical value ($\delta_x = \sqrt{3}a$), and the "slip" is facilitated by gliding of strain solitons. Alternatively, by increasing the pulling force, the GNR remains "stuck" until the force reaches the peak force (point 2) at which point the GNR would "slip" unstably under the force control.

Unlike the normal (adhesive) interactions in peeling (Fig. 3), where the characteristic length is very small ($\lambda_z \sim 0.32$ nm), the characteristic length for the shear interactions in sliding is much larger ($\lambda_x \sim 4.85$ nm) and thus more relevant for relatively short GNRs. Based on Eq. (20), the strain in a soliton scales with a/λ_x. Within each strain soliton, the relative displacement scales with the

---

[2] Some resistance to soliton gliding may exist due to the discreteness of the graphene lattice but is neglected in the continuum model. Future studies may consider including the resistance by a dissipative term for the energy dissipation associated with frictional sliding and soliton gliding.
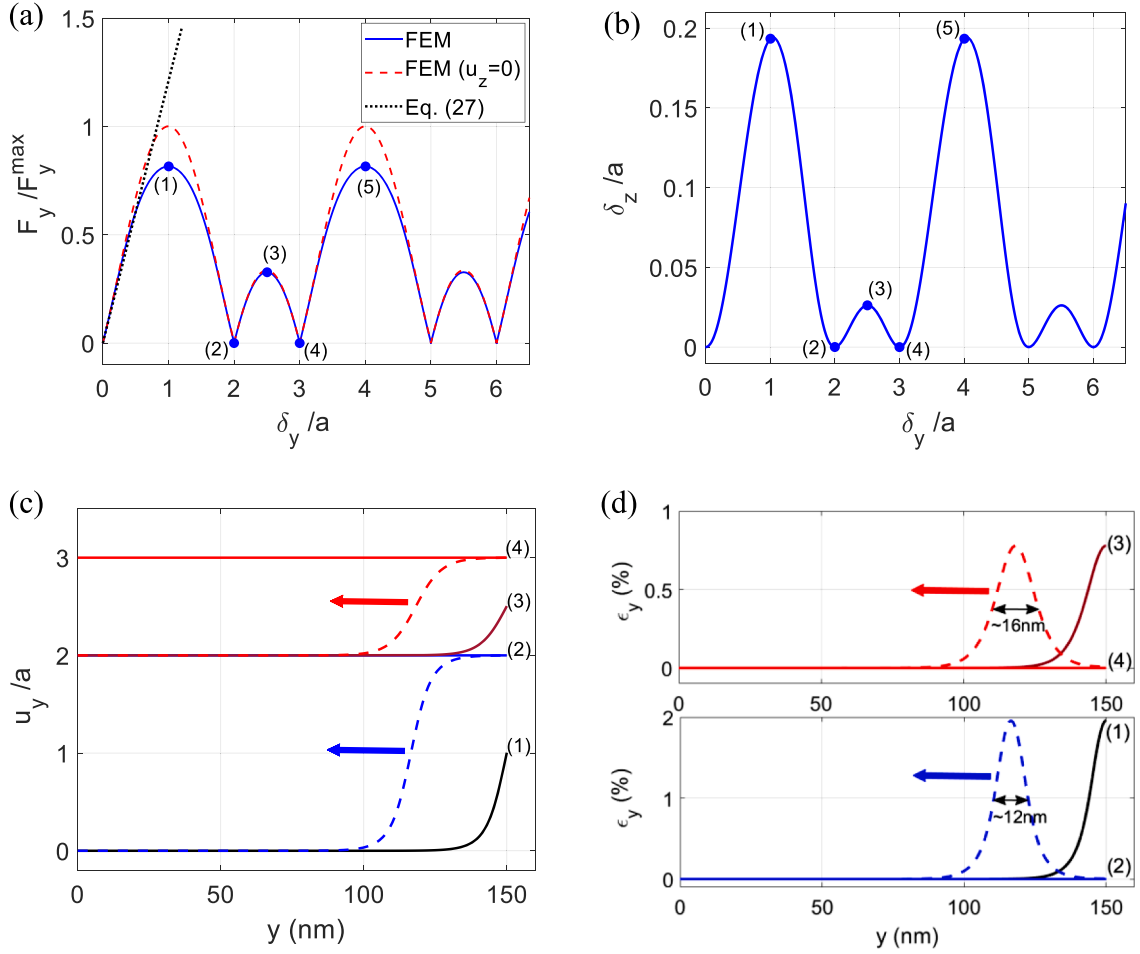
Fig. 6. Simulation of 1D sliding of an armchair GNR ($L = 150$ nm and $b = 1$ nm) in the y direction with constrained lateral displacement. (a) Normalized pulling force, and (b) normal displacement of the pulling end as a function of the pulling displacement, where the force is normalized by the predicted maximum force in Eq. (32). (c) Evolution of the sliding displacement, and (d) the corresponding axial strain distributions. The dashed lines in (c) and (d) show the displacement and strain of two different strain solitons.

bond length a. Hence the width of each strain soliton scales with λ_x. The numerical results in Fig. 4d show that the full width at half maximum (FWHM) of the strain soliton is ~14 nm (roughly 3 times of λ_x). As a result, the sliding behavior becomes dependent on the ribbon length (L) if the length is comparable to or less than ~50 nm, as shown in Fig. 5a. It is found that the initial stiffness (K_x) remains a constant for GNRs with $L > 10$ nm (roughly 2 times of λ_x) but decreases for shorter GNRs (Fig. 5b), as predicted by the linear solution in Eq. (27). Moreover, the peak pulling force follows a similar trend and remains a constant for GNRs with $L > 20$ nm. Notably, for GNRs of intermediate lengths ($10 < L < 50$ nm), there is a sudden drop of the pulling force after the peak, implying a snap instability (see Figs. S2a and S3 in SI). We believe that the instability occurs because the size of the strain soliton is comparable to the ribbon length for $10 < L < 50$ nm, so that the strain soliton interacts with the free end of the GNR and becomes unstable before it is fully developed. In contrast, for a relatively short GNR ($L \leq 5$ nm), the pulling force varies smoothly, approximately following a sinusoidal function of the pulling displacement, which suggests that the short GNR slides like a rigid flake with minimal deformation (see Fig. S4 in SI). In the case of uniform sliding of a rigid GNR, the peak pulling force increases linearly with the ribbon length ($\sim \tau_{xm}bL$), which is in close agreement with the numerical results (Fig. 5b) only for short GNRs ($L \leq 5$ nm).

For 1D sliding of a relatively long GNR ($L = 150$ nm) in the y direction (armchair) with the lateral displacement constrained ($u_x = 0$), the pulling force varies periodically with the pulling displacement (Fig. 6a), with a period of $3a$ corresponding to the structural periodicity along the armchair direction of the graphene lattice. Similar to 1D sliding in the x direction, the pulling force first increases linearly as predicted by the linear solution in Eq. (27) (same for sliding in the y direction) and reaches a peak force at $\delta_y = a$ (AA stacking). Subsequently, the pulling force drops to nearly zero at $\delta_y = 2a$ (AB stacking) and then rises up to a lower (secondary) peak at $\delta_y = 2.5a$ (saddle point). Compared to the prediction in Eq. (32), the primary peak force is about 20% lower than F_y^{max}, due to the normal displacement ($u_z \neq 0$), while the secondary peak force agrees closely with the prediction of $F_y^{max}/3$. The effect of the normal displacement on the primary peak force is thus more significant for sliding in the y direction than for sliding in the x direction (Fig. 4a).
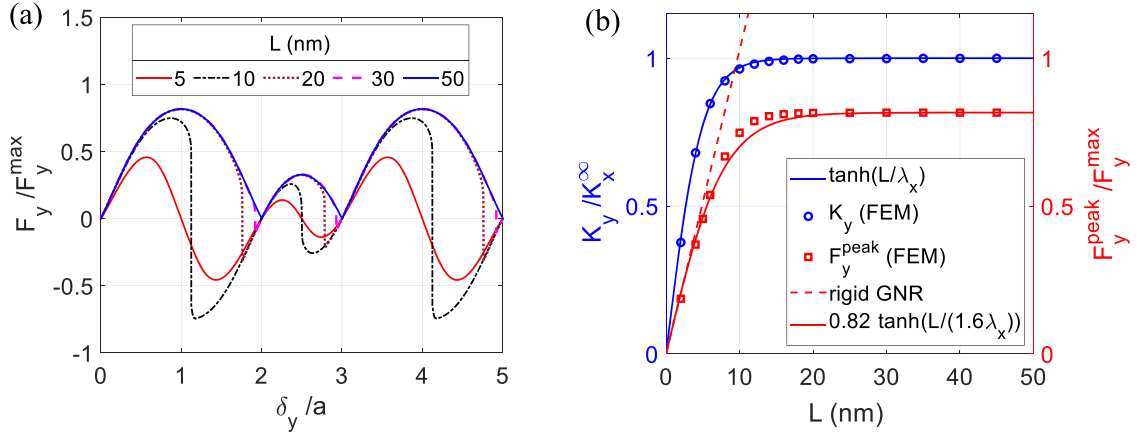
Fig. 7. Effects of the ribbon length on 1D sliding of armchair GNRs in the *y* direction with constrained lateral displacement. (a) Normalized pulling force as a function of the pulling displacement with different GNR lengths. (b) Normalized initial sliding stiffness (left axis) and the primary peak force (right axis) versus the GNR length.

Indeed, the magnitude of the normal displacement ($\sim 0.2a$; Fig. 6b) is almost twice of that for sliding in the x direction.

Similar to 1D sliding in the *x* direction, the sliding displacement in the y direction follows a stick-slip pattern (Fig. 6c and Fig. S2b), with "slips" facilitated by gliding of strain solitons (Fig. 6d). Interestingly, two kinds of strain solitons alternate for the 1D sliding in the y direction. The primary strain soliton forms first at a critical displacement of $2a$, with a peak strain of $\sim 2\%$, slightly lower than the prediction by Eq. (30) due to the normal displacement. Subsequently, at another critical displacement of $3a$, a secondary soliton forms with a peak strain of $\sim 0.8\%$ (1/3 of ε_{ym}) as predicted by Eq. (30). The FWHM width is ~ 12 nm for the primary soliton and is ~ 16 nm for the secondary soliton. We note that which soliton forms first depends on the starting position of the GNR with respect to the substrate. If started from the point (2) in Fig. 6(a), which also corresponds to AB stacking, the secondary soliton would form first, followed by the primary soliton. In this case, under force control, we would expect a small "slip" at the point (3) and then an unstable "slip" at the point (5).

Fig. 7 shows the effects of the ribbon length (*L*) on the 1D sliding of armchair GNRs in the *y* direction. Similar to the 1D sliding in the x direction, the sliding behavior becomes dependent on the ribbon length when $L < 50$ nm (see Figs. S2b, S5 and S6 in SI). As predicted analytically in Section 3.2, the initial stiffness is identical to that for sliding in the x direction as given in Eq. (27), which remains a constant for $L > 10$ nm. The primary peak force remains a constant for $L > 20$ nm. With no constraint on the normal displacement, the peak force for a relatively long ribbon ($L > 20$ nm) is about 20% lower than the predicted maximum force in Eq. (32). For a very short GNR (e.g., $L = 5$ nm), the sliding is nearly uniform (see Fig. S6) and the primary peak force is linearly proportional to the ribbon length ($\sim \tau_{ym}bL$).

5.2.2. Unconstrained sliding

Next, we consider sliding of GNRs without lateral constraint. In this case, while the pulling force is applied at one end of the GNR in the axial direction only (Fig. 1b), the displacements are allowed in all three directions. Remarkably, Fig. 8a shows that the pulling force as a function of the pulling displacement in the x direction changes significantly from that for 1D sliding with lateral constraint ($u_y = 0$) for a relatively long GNR ($L = 150$ nm). While the initial stiffness remains the same, the peak force is much lower and the variation period ($\sqrt{3}a/2$) is exactly half of the constrained case. Meanwhile, the lateral displacement at the pulling end (δ_y) oscillates between 0 and $a/2$ with a period of $\sqrt{3}a$ (Fig. 8b). As a result, the magnitude of the in-plane displacement is exactly one bond length (*a*) at point (2). It is noted that the normal displacement (u_z) during the unconstrained sliding is much smaller (in the order of 0.001 nm, about 10 times smaller than that in the constrained 1D sliding).

For a narrow GNR (e.g., with a width $b \sim 1$ nm), it is found that $\tau_y \approx 0$ during sliding in the x direction. Then, by Eq. (7) we have approximately

$$2\cos\left(\frac{G_1(u_y - a)}{2}\right) + \cos\left(\frac{\sqrt{3}}{2}G_1 u_x\right) = 0. \tag{34}$$

Substituting Eq. (34) into Eq. (6), we obtain

$$\tau_x = \frac{\sqrt{3}}{4}U_{1e}G_1 \sin\left(\sqrt{3}\,G_1 u_x\right) = \frac{1}{2}\tau_{xm}\sin\left(\sqrt{3}\,G_1 u_x\right). \tag{35}$$

Comparing Eq. (35) to Eq. (16), we note that the periodicity of the shear traction changes to half of the constrained case ($u_y = 0$) and the maximum shear traction reduces to half as well. On the other hand, the initial stiffness (k_x) for the shear interaction remains the same for small displacement ($u_x \ll a$), and so does the characteristic length scale (λ_x) for sliding as well as the initial sliding stiffness (K_x). With Eq. (35), the maximum strain is predicted to be half of that in Eq. (20) and correspondingly the maximum force is half of that
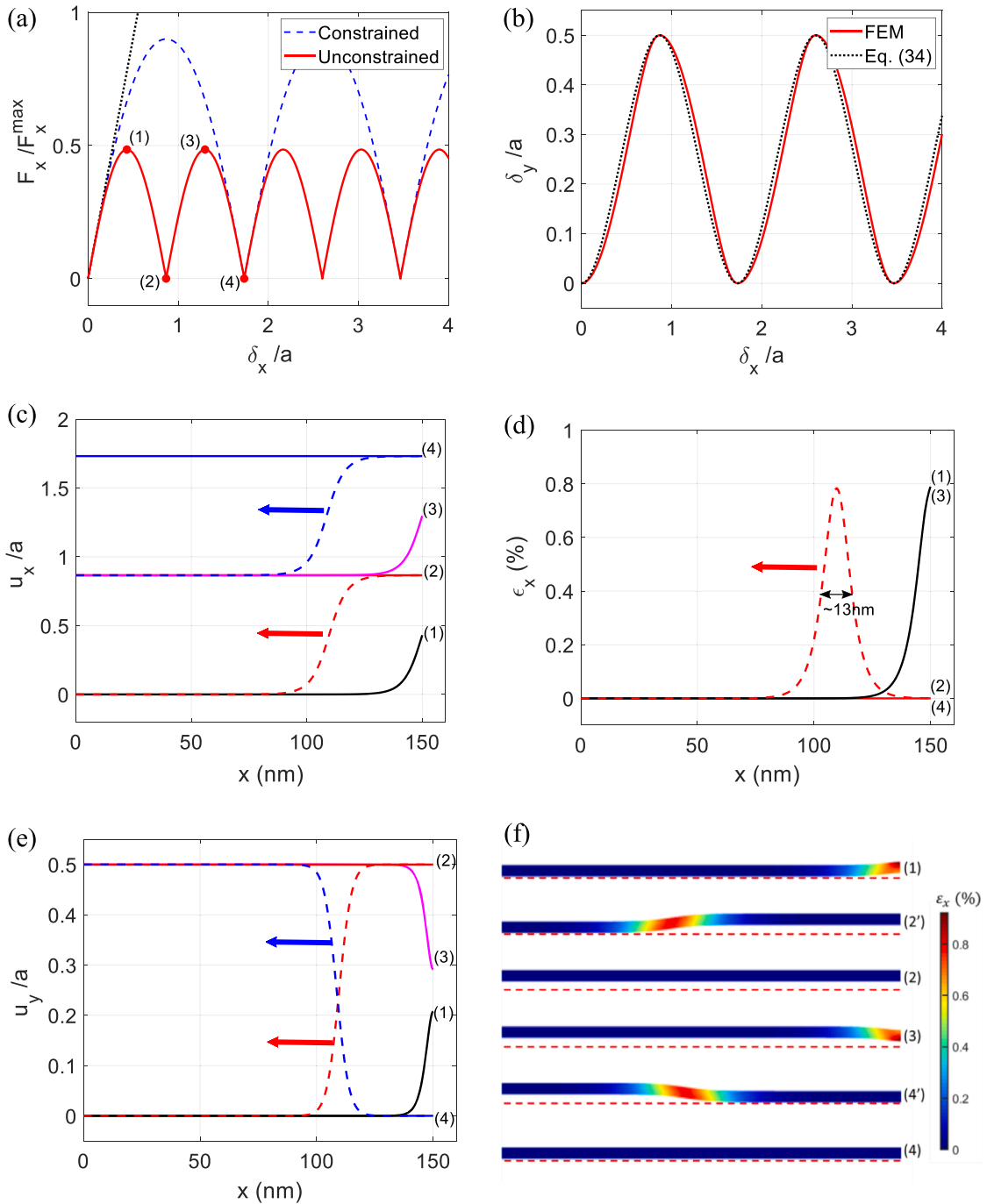
Fig. 8. Unconstrained sliding of a zigzag GNR ($L = 150$ nm and $b = 1$ nm) in the x direction. (a) Normalized pulling force and (b) lateral displacement (δ_y) at the pulling end of the GNR, versus the pulling displacement (δ_x). (c) Evolution of the axial displacement, (d) the axial strain, and (e) the lateral displacement of the GNR. (f) The axial strain distribution contours in the GNR at different pulling displacements. Note that, to enhance visual perception, the lateral displacement u_y is multiplied by a factor of 10 in (f).

in Eq. (22). Moreover, Eq. (21) becomes

$$F_x = b\sqrt{\frac{\tau_{xm}Et}{\sqrt{3}G_1}}\left[1 - \cos\left(\sqrt{3}\,G_1\delta_x\right)\right],\tag{36}$$

which predicts the pulling force as function of the pulling displacement for the unconstrained sliding of a narrow GNR in the x di-
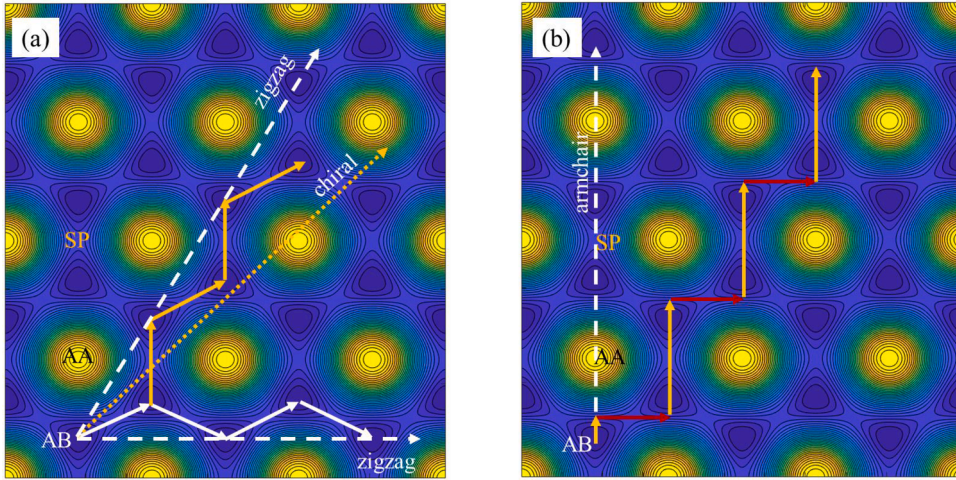
Fig. 9. Different sliding trajectories over the interlayer energy landscape: (a) Sliding in the zigzag directions ($\theta = 0$ or $60°$) and a chiral direction ($\theta = 45°$); (b) Sliding in the armchair direction ($\theta = 90°$). The dashed lines indicate 1D sliding in the zigzag and armchair directions. The solid lines are for unconstrained sliding with zigzag or stair-like paths.

rection. Evidently, the numerical results in Fig. 8a are in close agreement with Eq. (36), and the lateral end displacement in Fig. 8b follows Eq. (34) closely. The peak force in Fig. 8a is $0.485F_x^{peak}$, about 3% lower than the prediction by Eq. (36) due to the presence of a small normal displacement (u_z).

The sliding displacement u_x (Fig. 8c) shows a stick-slip pattern similar to the 1D sliding in Fig. 4c, but the critical displacement is reduced to half ($\sqrt{3}a/2$). Correspondingly, the strain soliton formed at the critical displacement (Fig. 8d) has a smaller peak strain ($\sim 0.8\%$) and a slightly smaller FWHM (~ 13 nm). In addition to the sliding displacement in the x direction, the concomitant lateral sliding of the GNR is shown in Fig. 8e. Following the lateral displacement of the pulling end (Fig. 8b), the entire GNR oscillates laterally between 0 and $a/2$, similar to snake-like sliding in fully atomistic simulations (Ouyang et al., 2018). As the strain soliton glides, the lateral displacement (u_y) undergoes a sharp transition (Fig. 8e). The deformation and strain distributions in the GNR (Fig. 8f) show that the strain soliton is primarily tensile with a small kink due to lateral bending.

The snake-like sliding behavior shown in Fig. 8 may be understood from an energetic consideration. Fig. 9a shows the energy landscape for the interlayer potential (assuming $u_z = 0$), where the lowest energy corresponds to AB stacking and the highest energy corresponds to AA stacking of the GNR on graphene. Starting from an equilibrium position of AB stacking, the constrained 1D sliding in the x-direction (zigzag) is represented by a straight dashed line, passing through a relatively high energy barrier between two positions of AB stacking. With lateral displacement, however, a zigzag path is followed with a lower energy barrier at the saddle point between adjacent AB stacking positions. As a result, the GNR slides with a lower resistance (friction) by the snake-like behavior.

For unconstrained sliding in the y direction (armchair), we assume that $\tau_x \approx 0$ for a narrow GNR (e.g., with a width $b \sim 1$ nm). Then, by Eq. (6) we have approximately

$$\cos\left(\frac{G_1(u_y - a)}{2}\right)\sin\left(\frac{\sqrt{3}}{2}G_1 u_x\right) = 0. \tag{37}$$

Eq. (37) suggests that the lateral displacement would take discrete values, $u_x = \pm\frac{\sqrt{3}}{2}na$ (for $n = 0, 1, 2, \ldots$) unless $\cos\left(\frac{G_1(u_y-a)}{2}\right) = 0$. Therefore, the lateral displacement may jump between the discrete values when $u_y = \frac{1}{4}(3n-2)a$ (for $n = 1, 3, \ldots$). Corresponding to each lateral jump, the shear traction by Eq. (7) switches between two branches:

$$\tau_y = -G_1 U_{1e}\left[\sin(G_1(u_y - a)) \pm \sin\left(\frac{G_1(u_y - a)}{2}\right)\right]. \tag{38}$$

Comparing to Eq. (28), the shear traction in Eq. (38) changes sign at each jump and as a result, the period of the shear traction becomes $1.5a$, half of the period in Eq. (28). The maximum shear traction is lowered to $G_1 U_{1e}$ or $0.568\tau_{ym}$, while the initial stiffness of the shear interactions for a small sliding displacement ($u_y \ll a$) is unaffected.

Substituting Eq. (38) into Eq. (11), we obtain

$$Et\varepsilon_y\frac{d\varepsilon_y}{du_y} = -U_{1e}G_1\left[\sin(G_1(u_y - a)) \pm \sin\left(\frac{G_1(u_y - a)}{2}\right)\right]. \tag{39}$$

Integrating Eq. (39) yields
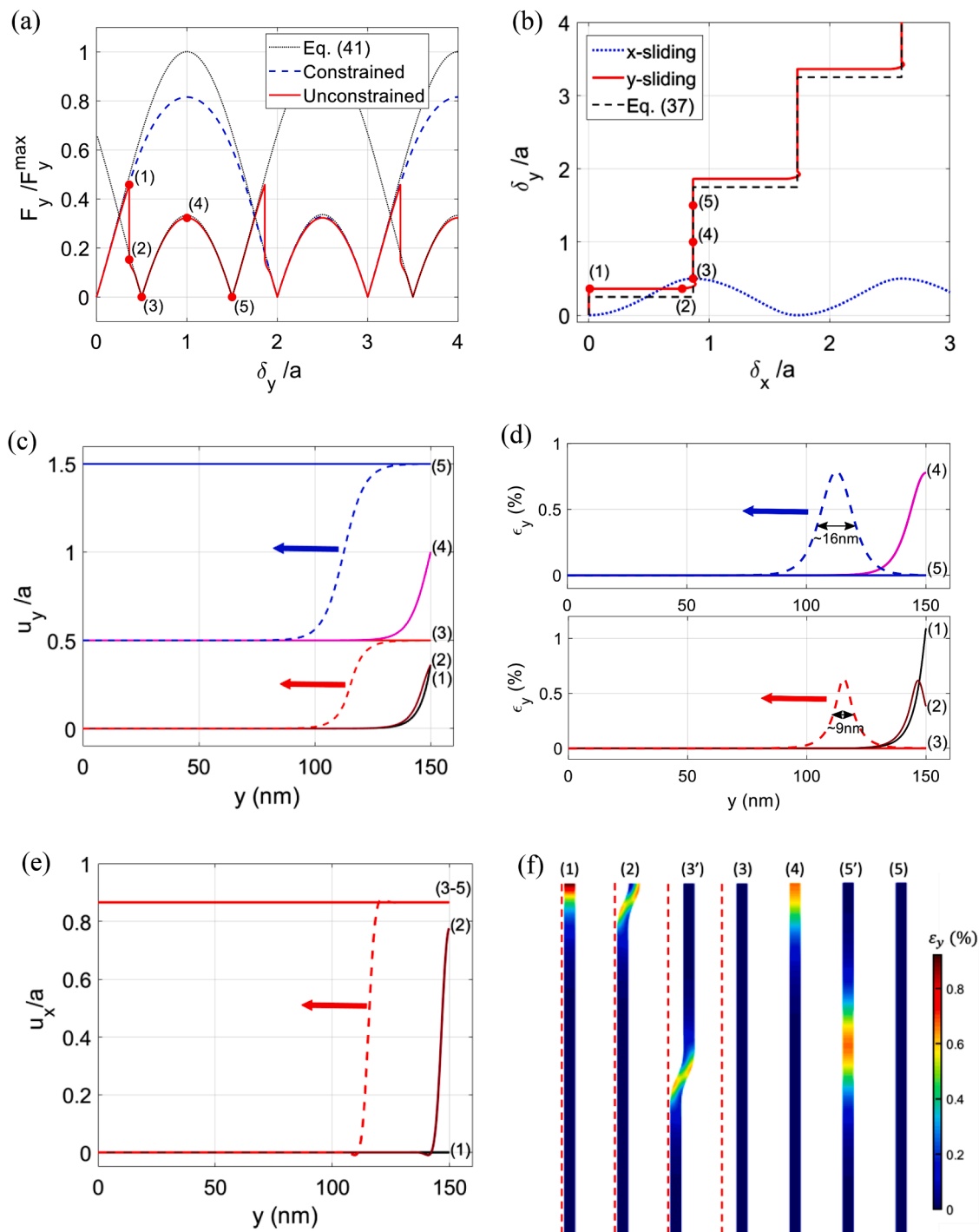
Fig. 10. Unconstrained sliding of an armchair GNR ($L = 150$ nm and $b = 1$ nm) in the y direction. (a) Normalized pulling force and (b) lateral displacement (δ_x) at the pulling end of the GNR, versus the pulling displacement (δ_y). (c) Evolution of the axial displacement, (d) the corresponding axial strain, and (e) the lateral displacement of the GNR. (f) The axial strain distribution contours in the GNR at different pulling displacements. To enhance visual perception, the lateral displacement (u_x) is multiplied by a factor of 10 in (f).

$$\varepsilon_y = \sqrt{\frac{2U_{1e}}{Et}}\left[\cos(G_1(u_y-a)) \pm 2\cos\left(\frac{G_1(u_y-a)}{2}\right) + \frac{3}{2}\right]^{1/2}.$$ (40)

Following Eq. (40), we obtain the pulling force (F_y) at the front end of the GNR as a function of the pulling displacement (δ_y) for the unconstrained sliding:

$$F_y = b\sqrt{2EtU_{1e}}\left[\cos(G_1(\delta_y-a)) \pm 2\cos\left(\frac{G_1(\delta_y-a)}{2}\right) + \frac{3}{2}\right]^{1/2}.$$ (41)

Remarkably, the two branches of the pulling force in Eq. (41) intersects at $\delta_y = \frac{1}{4}(3n-2)a$ (for $n = 1, 3, \ldots$), corresponding to the jumps in the lateral displacement. As shown in Fig. 10a, by switching between the two branches, the pulling force takes the lower value of the two. Comparing to Eq. (31), the primary peak force in Eq. (41) is lowered to $b\sqrt{EtU_{1e}}$ or $F_y^{max}/3$, same as the secondary peak force in Eq. (31), while the period of the pulling force variation with respect to the pulling displacement (δ_y) becomes $1.5a$, half of the period in Eq. (31). Similarly, the strain in Eq. (40) switches between two branches, and the maximum strain is lowered to $\varepsilon_{ym}/3$, same as the secondary (local) maximum in Eq. (30).

The above predictions for unconstrained sliding in the y direction (armchair) are compared to the FEM results in Fig. 10 for a relatively long and narrow GNR ($L = 150$ nm and $b = 1$ nm). The pulling force from FEM follows the two-branch solution in Eq. (41) closely in Fig. 10a, except that the switch between the two branches is slightly delayed, resulting in a higher peak force and a sudden drop of the force after each switch. The delayed switch is consistent with the delayed jump of the lateral displacement at the pulling end (δ_x) in Fig. 10b. Interestingly, while each jump in principle can go either way (left or right), the numerical results (Fig. 10b) show all jumps in the same direction (to the right) incidentally. Each jump of the lateral displacement corresponds to a sudden drop of the pulling force in Fig. 10a.

The sliding displacement u_y (Fig. 10c) shows a similar stick-slip pattern to the constrained 1D sliding in Fig. 6c, but with different critical displacements. The first critical displacement is $0.5a$ as opposed to $2a$ for 1D sliding (Fig. 6c), while the second critical displacement is $1.5a$ as opposed to $3a$ for 1D sliding. At each critical displacement (point 3 or 5 in Fig. 10a), a strain soliton forms and glides (Fig. 10d) to facilitate the "slip" of the GNR. Here, the second strain soliton is similar to that in the 1D sliding (Fig. 6d), with a peak strain of $\sim 0.8\%$ and a FWHM width of ~ 16 nm. However, the first strain soliton in Fig. 10d has a lower peak ($\sim 0.6\%$) and a smaller FWHM (~ 9 nm). Again, which soliton forms first depends on the starting position of the GNR (e.g., point 3 or 5 in Fig. 10a).

Interestingly, the jump in the lateral displacement (point 1 to 2) precedes the formation of the first soliton (point 3). As shown in Fig. 10e, the lateral jump leads to a kink near the pulling end, but the kink does not glide away until the first strain soliton forms at point 3 ($\delta_y = 0.5a$). Thus, the GNR remains "stuck" and straight until point 1, forms a kink at the pulling end (point 2), and then "slips" at point 3 with the strain soliton and the kink gliding simultaneously. Subsequently, another strain soliton forms at point 5 (Fig. 10d), with no kink, which glides in the same way as for 1D sliding (Fig. 6d). Therefore, two kinds of strain solitons alternate to form during unconstrained sliding in the y direction, one with a small kink and the other with no kink. The strain distributions in the GNR (Fig. 10f) shows that both strain solitons are primarily tensile.

The sliding behavior shown in Fig. 10 may be understood from an energetic consideration, as shown in Fig. 9b. Starting from an equilibrium position of AB stacking, 1D sliding in the y-direction (armchair) is represented by a vertical dashed line, passing through both AA stacking and saddle points (SP) as two different energy barriers. With lateral displacement, however, a stair-like path is followed, circumventing the higher energy barrier of AA stacking. At point 3 (Fig. 10b), the pulling end of the GNR reaches the nearest point of AB stacking, with displacements in both x and y directions, and the magnitude of the displacement is exactly one bond length (a). From point 3 to point 5, the displacement is one bond length (a) in the y direction only, reaching another point of AB stacking. As a result, the GNR slides with a lower resistance (friction) and a significantly lower peak force than for the 1D sliding. Compared to Fig. 9a, the energy barrier across the saddle point is the same for sliding in both x and y directions, but the peak pulling force is slightly higher for sliding in the y direction due to delayed jump in the lateral direction.

Besides the zigzag (x) and armchair (y) directions, it is also possible for GNRs with chiral edges to slide in a chiral direction (e.g., $30°$ $< \theta < 60°$). Considering the six-fold symmetry of the graphene lattice, a representative chiral direction is shown in Fig. 1 with $\theta = 45°$. It is found that sliding of such a chiral GNR follows a path similar to that of a zigzag GNR sliding in the x direction ($\theta = 0$ or $60°$ in Fig. 9a). Interestingly, as shown in Fig. 11a, the peak pulling force is nearly identical to that for sliding in the x direction, $F_\theta^{peak} \approx 0.5F_x^{max}$, although the periodic variation with respect to the pulling displacement is different. Fig. 11b shows that the end of the GNR approximately follows a zigzag path with two periods: $a\cos\left(\frac{\pi}{12}\right)$ and $a\cos\left(\frac{\pi}{4}\right)$, along the pulling direction ($\theta = 45°$). The sliding trajectory is illustrated approximately in Fig. 9a over the energy landscape. Similar to sliding in the armchair direction, two different strain solitons alternate as they form and glide to facilitate the stick-slip sliding (see Fig. S7 in SI). Both solitons are primarily tensile and accompanied by lateral bending (kink) of the GNR, but they are different in terms of the maximum tensile strain and the FWHM width.

Effect of ribbon length. Similar to the constrained 1D sliding Figs. 5 and 7), the unconstrained sliding behavior becomes dependent on the ribbon length (L) if the length is comparable to or less than ~ 50 nm. Fig. 12 shows the peak pulling force as a function of the GNR length for unconstrained sliding in the x and y directions (also see Figs. S8 and S9 in SI). The dependence of the peak force on the ribbon length is similar to fully atomistic simulations (Ouyang et al., 2018), with an initial linear rise and a plateau beyond a characteristic length of around 10 to 20 nm. The amplitude of the plateau peak force (per unit width) is ~ 3.83 N/m ($0.458F_y^{peak}$) for the armchair GNRs by the present model ($b = 1$ nm), in excellent agreement with MD simulations by Ouyang et al. (2018), which was ~ 3.89 N /m
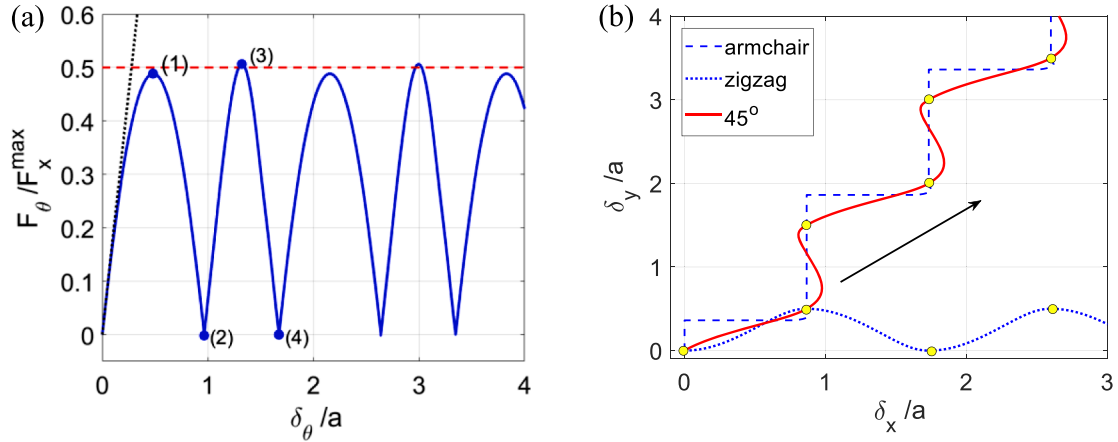
Fig. 11. Unconstrained sliding of a chiral GNR ($\theta = 45°$, $L = 150$ nm and $b = 1$ nm). (a) Normalized pulling force versus the pulling displacement, and (b) the sliding trajectory of the pulling end of the GNR, in comparison with those for the zigzag and armchair GNRs. The yellow dots indicate the locations of AB stacking.

(~ 2.72 nN for GNRs with a width of 0.7 nm). The amplitude of the plateau peak force is lower for the zigzag GNRs, ~ 2.7 N /m ($0.485F_x^{peak}$). For short GNRs ($L < 5$ nm), the peak force is found to be linearly proportional to the contact area as shown by the dashed and dotted lines in Fig. 12, with a shear strength of $0.5\tau_{xm}$ and $0.568\tau_{ym}$ as predicted by Eqs. (35) and ((38) for the zigzag and armchair GNRs, respectively. The short GNRs slide almost uniformly like a rigid flake, but following the 2D trajectories (see Figs. S8 and S9 in SI) similar to those illustrated in Fig. 9, which effectively reduces the shear strength by half.

Effects of ribbon width. Fig. 13 shows the peak pulling force as a function of the GNR width for unconstrained sliding in the x (zigzag) and y (armchair) directions. For both zigzag and armchair GNRs, the peak pulling force is approximately linear with respect to the ribbon width, $\sim \frac{b}{a}\sqrt{Ete_1}$, which is around 2.7 and 3.83 N/m for the zigzag and armchair GNRs ($L > 20$ nm), respectively. For armchair GNRs sliding in the y direction, the normalized peak pulling force per unit width increases slightly as the ribbon width increases (see Fig. S10 in SI). We note that the edge effects on the elastic properties and vdW interactions could be prominent for narrow GNRs, which may be of interest for a future study. Without considering the edge effects, the peak pulling force for sliding of relatively long GNRs ($L > 20$ nm) is nearly independent of the ribbon length (Fig. 12) but depends on the ribbon width quasi-linearly (Fig. 13).

Unlike the constrained 1D sliding, where the GNR remains straight without any lateral displacement, the unconstrained sliding is accompanied by lateral displacement for both zigzag and armchair GNRs as well as the chiral GNRs. For a narrow GNR (e.g., $b \sim 1$ nm), the lateral displacement leads to in-plane bending (see Figs. 8d and 10d). However, as the GNR width increases, the in-plane bending stiffness increases, and as a result, the normalized peak pulling force (per unit width) increases slightly. For a relatively wide GNR ($b > 10$ nm), the strain soliton with lateral displacement typically nucleates from a corner of the pulling end and forms a band of localized strain with an angle of $\pm 60°$ from the pulling direction (Fig. 14). It is found that the strain soliton for sliding in the zigzag direction is primarily tensile, with a small shear strain component (γ_{xy}). The relative displacement across the soliton has an angle of approximately $\pm 30°$ from the x direction (Fig. 14a), and hence the strain soliton is a mixed type with both tensile and shear strain components with respect to the inclined soliton orientation. For sliding in the armchair direction, two types of strain solitons alternate, one of which is a tensile strain soliton (with no lateral displacement) and the other is primarily a shear strain soliton (except for the regions near the free edges of the GNR). As illustrated in Fig. 14d, the relative displacement across the shear strain soliton is parallel to the soliton, resembling a shear band (Tvergaard et al., 1981). However, the strain becomes primarily tensile near the free edges, dictated by the traction-free boundary condition. The boundary effect dominates for a narrow GNR (e.g., $b < 10$ nm), and thus the shear strain soliton forms only in relatively wide GNRs. Both tensile and shear strain solitons have been observed in graphene bilayers (Alden et al., 2013; Jiang et al., 2016; Yoo et al., 2019; Kim et al., 2020). Formation of shear strain solitons in twisted graphene bilayers has been simulated by Zhang and Tadmor (2018) using a discrete–continuum method. By applying a tensile strain to one of the graphene layers, Kumar et al. (2016) simulated formation of strain solitons similar to that in Fig. 14a (zigzag), although their solitons were trapped in the graphene bilayer due to different boundary conditions.[3] The present study shows that the stick-slip sliding of GNRs can be facilitated by formation and gliding of different types of strain solitons, depending on the pulling direction and the ribbon width. The shear strain soliton shown in Fig. 14d has a FWHM width of ~ 10 nm and a maximum strain of $\sim 0.9\%$, both comparing closely with atomic resolution STEM measurements (Alden et al., 2013).

---

[3] In Kumar et al. (2016), a uniaxial strain was applied to the lower graphene layer, whereas the upper layer was not subject to any external force other than the interactions with the lower layer. This is equivalent to the case with pulling forces applied to both ends of a GNR in opposite directions. As a result, strain solitons were trapped and more than one soliton can co-exist.
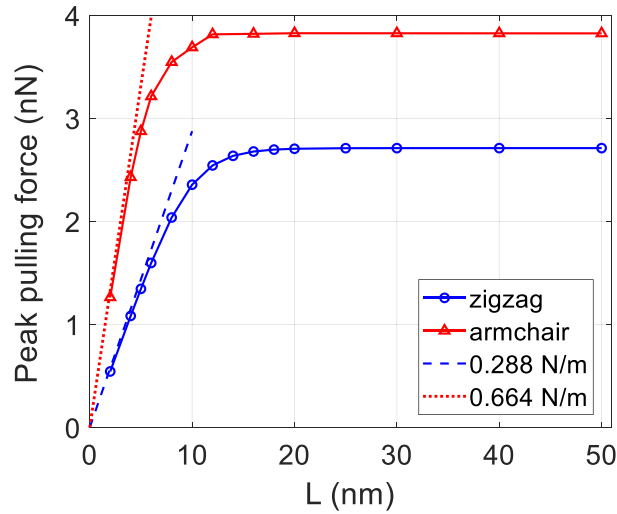
Fig. 12. Peak pulling force as a function of the GNR length for unconstrained sliding in the x (zigzag) and y (armchair) directions (ribbon width $b = 1$ nm).
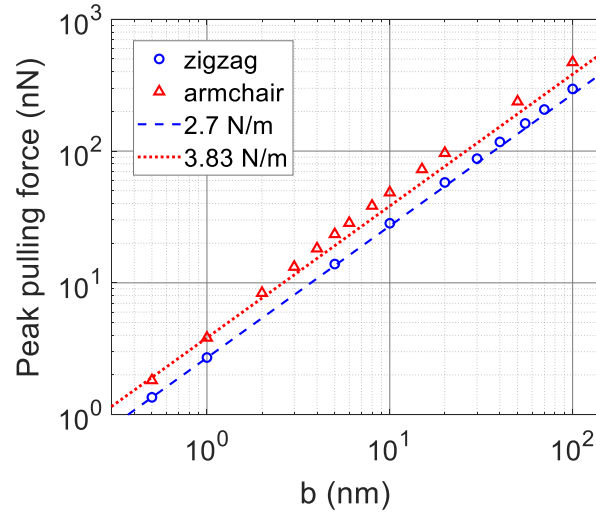
Fig. 13. Peak pulling force as a function of the GNR width for unconstrained sliding in the x (zigzag) and y (armchair) directions (ribbon length $L = 100$ nm).

5.3. Coupled peeling and sliding

5.3.1. Peeling with sliding

We consider two cases with coupled peeling and sliding of GNRs (Fig. 1c). For the first case, the GNR is picked up at one end with a normal peeling displacement (δ_z) while the in-plane displacements (δ_x and δ_y) are fixed at the same end, similar to a nano-peeling experiment using an atomic force microcopy (AFM) (Gigli et al., 2019a). Similar peeling experiments have also been conducted for other materials (Kovalchick et al., 2014). Unlike the case of simple peeling (no sliding) discussed in Section 5.1, the fixed in-plane displacements at the peeling end lead to sliding of the GNR during peeling and correspondingly, the reaction forces in the in-plane directions due to the shear interactions at the interface. On the other hand, if the contact between the GNR and its substrate is frictionless or superlubric as considered in Gigli et al. (2019b), the peeling force-displacement behavior would be exactly the same as the simple peeling case (Fig. 3), with frictionless sliding but no in-plane reaction forces.

Fig. 15a shows the forces at the peeling end versus the peeling displacement for a zigzag GNR. The peeling force (F_z) is drastically different from that in the case of simple peeling (Fig. 3a). While the initial stiffness is similar, ~14.4 N/m as predicted by Eq. (14), the peeling force reaches a higher peak followed by a sudden drop, signaling a stick-slip sliding during the peeling process. Indeed, the reaction force in the x direction (F_x) drops simultaneously, and the in-plane displacements (u_x and u_y) of the tail end (Fig. 15b) confirm the stick-slip sliding of the GNR at the same peeling displacement ($\delta_z \sim 0.6$ nm). Subsequently, as the peeling displacement increases,
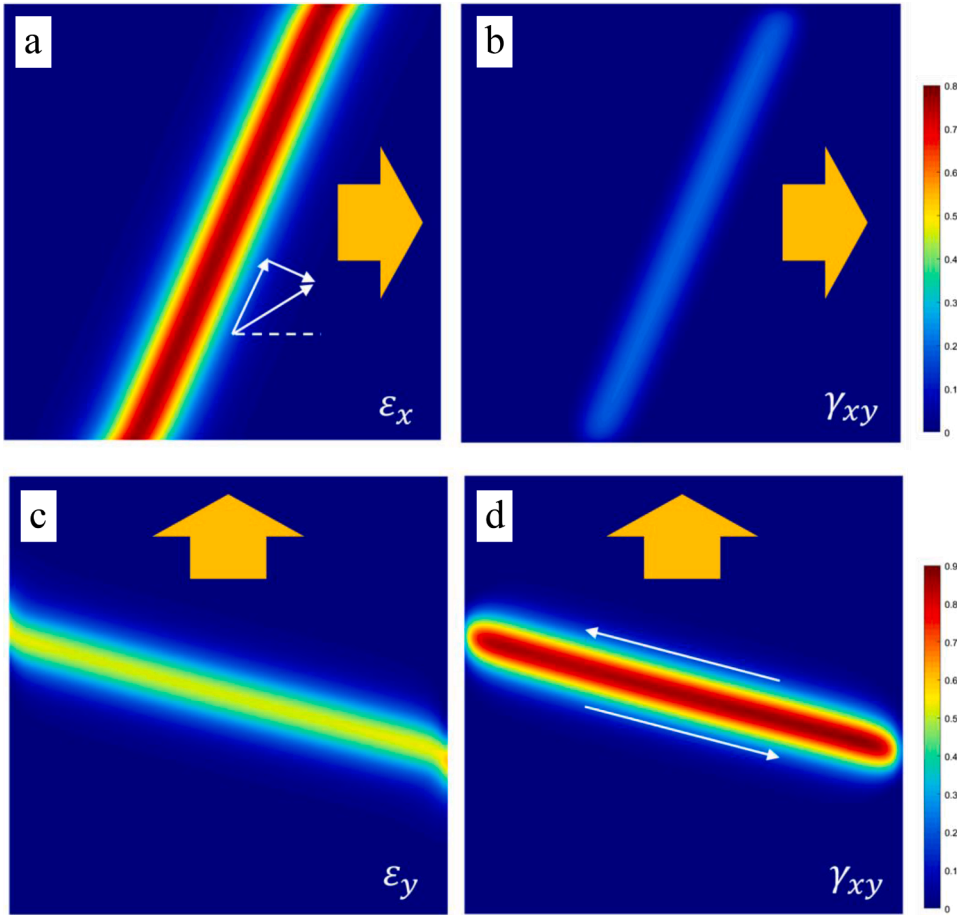
Fig. 14. Axial and shear strain distributions of the strain solitons formed in GNRs ($b = L = 100$ nm) during sliding in the (a, b) zigzag and (c, d) armchair directions. The color bars show strain in per cent.

both the peeling force and the axial reaction force periodically increase and drop, with each drop corresponding to a sudden slip at the tail end. Evidently, due to coupling with stick-slip sliding, the peeling force does not maintain a constant steady state value as expected from the classic peeling models (Rivlin, 1944; Kendall, 1975). Instead, the peeling force appears to peak at a constant level before each drop, approaching a steady state as the force drop becomes less significant at a larger peeling displacement. Meanwhile, the peak reaction force in the x direction approximately equals the peak pulling force for unconstrained sliding in Fig. 8a ($F_x^{peak} \sim 0.485 F_x^{max}$), whereas the reaction force in the y direction (F_y) becomes negligible after the second slip. The peeling force (F_z) and the axial reaction force (F_x) combine to yield a resulting force vector in the direction parallel to the detached GNR, with an angle θ from the x direction (Fig. 1c, and Fig. S11 in SI). Following an energetic consideration (Rivlin, 1944), the magnitude of the resulting force may be related to the adhesion energy (Γ_0) as[4]

$$F = \frac{\Gamma_0 b}{1 - \cos\theta}.$$

$$(42)$$

The slip occurs when the x-component of the force reaches the peak pulling force for sliding, namely

$$F_x^{peak} = \Gamma_0 b \frac{\cos\theta_c}{1 - \cos\theta_c},$$

$$(43)$$

which predicts a critical angle:

---

[4] As noted earlier, the effect of elastic strain energy in the GNR on the steady-state peeling force (Kendell, 1975) is negligible, because the in-plane stiffness of monolayer graphene ($Et = 345$ N/m) is much larger than the adhesion energy ($\Gamma_0 = 0.25$ N/m) and the peeling angle θ is relatively large ($\sim 20°$).
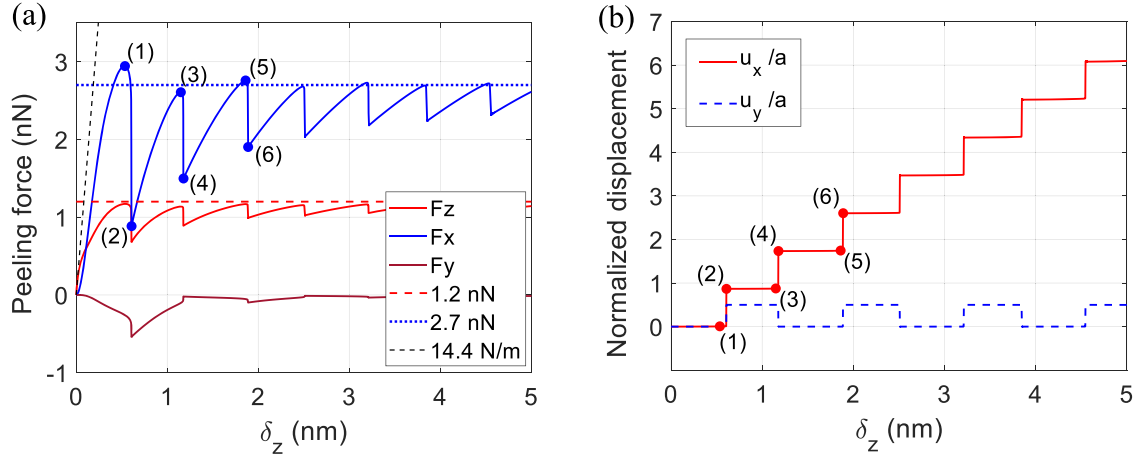
Fig. 15. (a) The peeling force (F_z) and reaction forces (F_x, F_y) versus the peeling displacement for a zigzag GNR ($L = 100$ nm and $b = 1$ nm), and (b) the sliding displacements at the tail end versus the peeling displacement.
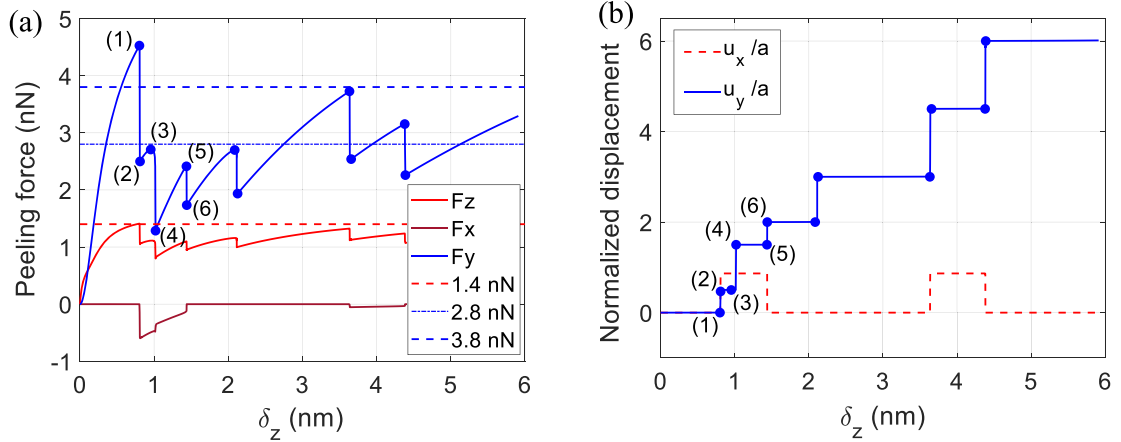
Fig. 16. (a) The peeling force and the reaction forces versus the peeling displacement for an armchair GNR ($L = 100$ nm and $b = 1$ nm), and (b) sliding displacements at the tail end versus the peeling displacement.

$$\cos\theta_c = \left(1 + \frac{\Gamma_0 b}{F_x^{peak}}\right)^{-1}. \tag{44}$$

With $F_x^{peak} = 0.485 F_x^{max} = 2.7b$ and $\Gamma_0 = 0.25$ J/m^2 for the GNR in the present model, we obtain the critical angle, $\theta_c = 24°$, which compares closely with the FEM results (Fig. S11b). Then, the corresponding peeling force at the peak is predicted as:

$$F_z^{peak} = F_x^{peak}\tan\theta_c = \Gamma_0 b\sqrt{1 + \frac{2F_x^{peak}}{\Gamma_0 b}}, \tag{45}$$

which yields 1.2 nN for $b = 1$ nm and agrees closely with the peak peeling force in Fig. 15a. This is remarkable, suggesting that the peeling force (F_z^{peak}) depends on both the normal and shear interactions via the adhesion energy (normal) and the stick-slip sliding (shear/friction). As a result, by measuring the peak peeling force and the critical angle, it is possible to determine both the adhesion energy (Γ_0) and the critical friction force for sliding (F_x^{peak}) by Eqs. (44) and (45). In contrast, for the case of simple peeling with no sliding (Section 5.1), both the peak and steady-state peeling forces are lower and related to the adhesion energy, independent of the shear interactions or friction.

Moreover, unlike the case of simple peeling in Section 5.1, which is independent of the GNR orientation, the fixed-end peeling depends on the GNR orientation due to coupling with stick-slip sliding. Fig. 16a shows the forces at the peeling end versus the peeling displacement for an armchair GNR, and the corresponding displacements at the tail end are show in Fig. 16b. Again, the signature of stick-slip sliding is noticeable with sudden jumps in both the forces and tail displacements. For the armchair GNR, two different types
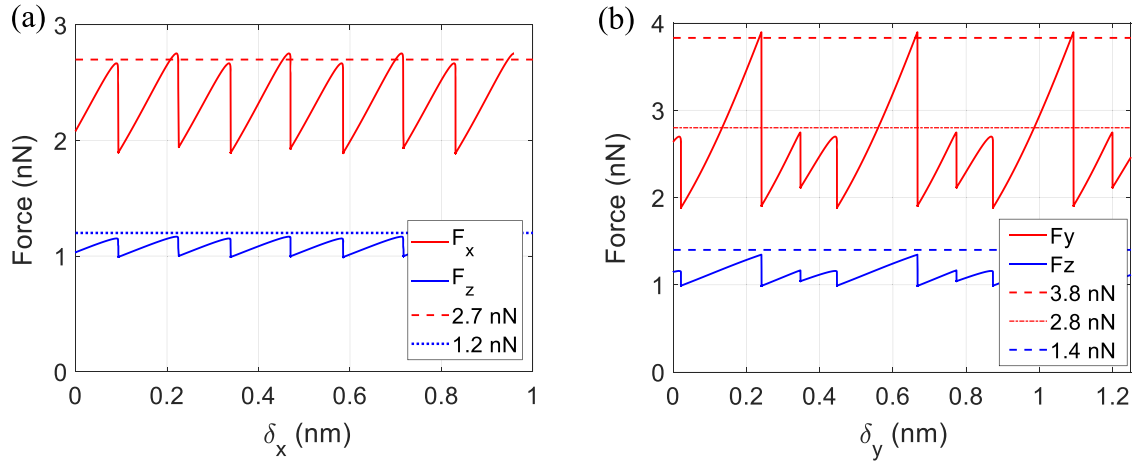
Fig. 17. The pulling force and the normal reaction force versus the pulling displacement of (a) a zigzag GNR and (b) an armchair GNR, both with the pulling end lifted at $\delta_z = 2\ nm$, $L = 100\ nm$, and $b = 1\ nm$.

of strain solitons have been noted for unconstrained sliding in Section 5.2.2, leading to two different peak pulling forces (Fig. 10a), $0.458F_y^{max}$ (~3.8 nN) and $0.333F_y^{max}$ (~2.8 nN) for $b = 1$ nm, with which we obtain two critical angles by Eq. (44), $\theta_c = 20°$ and $23°$. Then, the corresponding peak peeling forces are predicted by Eq. (45) as 1.4 and 1.2 nN, respectively. The predicted peak forces and critical angles are in generally good agreements with the numerical results (Fig. 16a and Fig. S12b), although some of the peak forces are either under or over-predicted due to the effect of the fixed-end boundary condition that either hinders or promotes formation of strain solitons with in-plane bending in opposite directions. Compared to the zigzag GNR of the same width ($b = 1$ nm), the primary peak peeling force (1.4 nN) is slightly higher for the armchair GNR. We note that the peeling and sliding behavior could be different for incommensurate interfaces, such as GNRs on gold, where a stick-slip motion along the ribbon axis was observed at the tail of the GNR but with no snake-like motion (Gigli et al., 2019a and 2019b). In the case of superlubric interfaces, $F_x^{peak} \approx 0$, so that $\theta_c \approx 90°$ from Eq. (44) and the peeling force $F_z^{peak} \approx \Gamma_0 b$ from Eq. (45), consistent with the observations by Gigli et al. (2019a and 2019b) for peeling of GNRs on gold.

5.3.2. Sliding with a lifted end

Kawai et al. (2016) studied the frictional and adhesive properties of GNRs on an Au(111) substrate by means of lateral manipulation using dynamic AFM in UHV at a low temperature (4.8 K). In their experiments, one end of the selected GNR was anchored to the AFM tip and dragged back and forth in a controlled way while the lateral reaction force was recorded as the friction force. Similar to their experiments, we consider sliding of GNRs on graphene with the pulling end lifted at a constant normal displacement (δ_z). Here, in addition to the pulling force, a normal reaction force (F_z) is required to maintain the normal displacement at the pulling end. As shown in Fig. 17, for both zigzag and armchair GNRs, the pulling force shows the characteristic stick-slip behavior and so does the normal reaction force. Compared to the unconstrained sliding in Section 5.2 (Figs. 8 and 10), the peak pulling forces are nearly identical, but the force profiles are quite different with abrupt drops. This difference can be attributed to the lifted end with a detached segment of GNR acting like an elastic spring pulling on the rest of the GNR, with the effective spring stiffness depending on the normal displacement (δ_z) of the lifted end. While in the experiments by Kawai et al. (2016) the GNRs were dragged to slide on an Au(111) substrate with different adhesion and friction, qualitatively similar stick-slip responses were observed both in the experiments and in MD simulations (Gigli et al., 2017 and 2018). An interesting comparison can be made with the MD simulations by Ouyang et al. (2018), where a few external springs were attached to the end of an armchair GNR. Similar to Fig. 17b, the MD simulations predicted two different peak pulling forces for an armchair GNR sliding on graphene, with an abrupt drop from each peak and a periodicity of about 0.42 nm between the primary peaks. The only notable difference is that, while there are two secondary peaks within each period in Fig. 17b, there was only one secondary peak in the MD simulations. This difference is likely due to the particular spring stiffness used in the MD simulations that is different from the effective stiffness here with a lifted end ($\delta_z = 2$ nm). Besides the pulling forces, the normal reaction force (F_z) has the same peaks as those in Figs. 15 and 16 for peeling with sliding, and the critical peeling angles for stick-slip are similar (see Figs. S13 and S14 in SI). Therefore, by measuring both the lateral and normal forces, the friction and adhesion properties of the GNR can be determined based on Eqs. (43) and (45).

6. Summary

This paper presents a continuum model for peeling and sliding of graphene nanoribbons (GNRs) on a graphene substrate with van der Waals (vdW) interactions, simulated by a finite element method using a periodic potential energy function. Numerical simulations and associated analyses reveal remarkably rich dynamics for peeling and sliding of GNRs. The main findings are summarized as follows.

- The simple 90-degree peeling of a relatively long GNR ($L > 5$ nm) is characterized by three key parameters: the initial stiffness, the peak force, and the steady-state force. The peeling behavior primarily depends on the normal (adhesive) interactions, with negligible sliding or shear interactions. In contrast, peeling with the end fixed in the in-plane directions leads to stick-slip sliding, with a higher peeling force and a critical peeling angle depending on both adhesion and friction.
- Stick-slip sliding is simulated as a result of formation and gliding of strain solitons in GNRs. Constraining the displacements in the normal and/or lateral directions would lead to higher pulling force in 1D sliding. In contrast, unconstrained sliding is typically accompanied by both lateral and normal displacements. Without considering the edge effects, the peak pulling force for sliding of relatively long GNRs ($L > 20$ nm) is nearly independent of the ribbon length but depends on the ribbon width quasi-linearly.
- The strain solitons are primarily tensile for narrow GNRs (e.g., $b \sim 1$ nm), with kinks due to lateral displacement. For relatively wide GNRs ($b > 10$ nm), the strain solitons are of mixed type with both tensile and shear strains in the zigzag GNRs, whereas tensile and shear strain solitons alternate to form in the armchair GNRs.
- Two cases with coupled peeling and sliding of GNRs are considered, peeling with a fixed end and sliding with a lifted end. Both illustrate the mixed-mode interactions with coupled adhesion and friction. A simple analysis is proposed, relating the measurable quantities in potential experiments to the adhesion and friction properties of GNRs.

Declaration of Competing Interest

The authors declare that they have no known competing financial interests or personal relationships that could have appeared to influence the work reported in this paper.

Acknowledgements

Appendix. Interactions between two graphene monolayers

The van der Waals (vdW) interactions between two carbon atoms in two graphene monolayers are modeled by the registry-dependent Kolmogorov-Crespi (KC) potential (Kolmogorov and Crespi, 2005), which has the following form:

$$V_{KC}\left(\vec{r}_{ij}, \vec{n}_i, \vec{n}_j\right) = e^{-\lambda\left(r_{ij}-z_0\right)}\left[C + f\left(\rho_{ij}\right) + f\left(\rho_{ji}\right)\right] - A\left(\frac{r_{ij}}{z_0}\right)^{-6}, \tag{A1}$$

where $\vec{r}_{ij}$ is a vector pointing from atom i in one monolayer to atom j in the other monolayer and $r_{ij} = |\vec{r}_{ij}|$; $\vec{n}_i$ and $\vec{n}_j$ are the unit normal vectors to the sp^2 planes in the vicinity of atoms i and j, respectively. The function $f(\rho)$ reflects the directionality of the interaction and takes the form:

$$f(\rho) = e^{-(\rho/\delta)^2}\left[C_0 + C_2(\rho/\delta)^2 + C_4(\rho/\delta)^4\right], \tag{A2}$$

where $\rho_{ij} = \sqrt{r_{ij}^2 - (\vec{n}_i \cdot \vec{r}_{ij})^2}$. For the carbon–carbon interactions in a graphene bilayer, the parameters of the KC potential take the following values: $C_0 = 15.71$ meV, $C_2 = 12.29$ meV, $C_4 = 4.933$ meV, $C = 3.030$ meV, $\delta = 0.578$Å, $\lambda = 3.629$Å^{-1}, $A = 10.238$ meV, and $z_0 = 3.34$Å.

Direct calculation of the interaction energy with Eq. (A1) is computationally expensive due to the long-range nature of vdW interactions. To reduce the computational cost, a continuum approximation may be used by assuming a uniform distribution of atoms and integrating the interaction energy between one atom and an infinite graphene layer (Zhang and Tadmor, 2017). However, such a continuum approximation depends only on the normal separation between the atom and the monolayer, independent of the translation of the atom in the tangential directions and hence registry independent. To address this limitation, we adopt the discrete–continuum (DC) method (Zhang and Tadmor, 2017) to calculate the interaction energy between one atom and one monolayer, namely

$$W_{DC}(x_i, y_i, z_i) = \sum_{j \in P} V_{KC}\left(r_{ij}\right) - \frac{5\gamma}{3}\left(\frac{z_0^2}{z_i^2 + r_{cut}^2}\right)^2, \tag{A3}$$

where (x_i, y_i, z_i) denotes the position of the atom i relative to the monolayer with the in-plane coordinate (x_i, y_i) (see Fig. A1) and the

normal separation z_i, $r_{ij} = \sqrt{(x_i - x_j)^2 + (y_i - y_j)^2 + z_i^2}$ is the distance between the atom i and another atom (j) in the monolayer within a region P where $r_{ij}^2 - z_i^2 \leq r_{cut}^2$, and r_{cut} is the cut-off radius that limits the range of the discrete summation. For the region outside the cut-off radius ($r_{ij}^2 - z_i^2 > r_{cut}^2$), the first term (short ranged) on the right-hand side of Eq. (A1) is ignored and the second term is integrated by the continuum approximation, giving rise to $\gamma = \frac{3}{10}\pi A \rho_s z_0^2 = 41.1$ meV/atom, where $\rho_s = 0.382$ atom/Å^2 (number of carbon atoms per unit area of graphene). As a result, the short-ranged interactions calculated by the summation in Eq. (A3) are registry dependent, whereas the long-ranged interactions are accounted for by the continuum approximation (registry independent). For the interactions between a carbon atom (in graphene) and a graphene monolayer, we take $r_{cut} = 20$ Å. To prevent discontinuities in the potential energy function, the discrete summation in Eq. (A3) is multiplied by a smoothing function φ:

$$\varphi = \begin{cases} 1 & r < r_{cut} - d \\ \frac{1}{2}\left[1 - \cos\left(\frac{r - r_{cut}}{d}\pi\right)\right] & r_{cut} - d < r < r_{cut} \\ 0 & r > r_{cut} \end{cases} \tag{A4}$$

where $d = 2$ Å is used for smoothing.

As shown in Fig. A1, the energy landscape for the carbon-graphene interaction is registry dependent with a hexagonal symmetry, dictated by the hexagonal lattice of graphene. For a constant normal separation (e.g., $z = 3.34$ Å), the minimum interaction energy is obtained when the carbon atom is located directly on top of the center of a hexagonal unit cell of graphene, while the maximum interaction energy is obtained when the atom is directly on top of a carbon atom of the graphene lattice. Moreover, saddle points of the energy landscape are obtained when the atom is on top of the midpoint of a carbon-carbon bond in graphene. The energy difference between the minimum and the maximum depends on the normal separation (z). At each in-plane location (x and y), the interaction energy depends on the normal separation (z), with a minimum that varies slightly with the in-plane location.

An analytical function was suggested for the spatial variation of the interlayer potential energy between two monolayers of 2D materials (including graphene) based on DFT calculations (Kumar et al., 2015 and 2016). Here, we assume a similar analytical form for the interaction energy between one carbon atom and one graphene monolayer, namely

$$W(x, y, z) = W_0(z) + 2W_1(z)\cos(G_1 y) + 4W_1(z)\cos\left(\frac{G_1 y}{2}\right)\cos\left(\frac{\sqrt{3}G_1 x}{2}\right), \tag{A5}$$

where $W_0(z)$ is the average interaction energy, $W_1(z)$ dictates the magnitude of the energy corrugation, and $G_1 = \frac{4\pi}{3a}$ is the magnitude of the reciprocal vector for the primitive unit cell of the monolayer. A similar interaction potential function was used by Verhoeven et al. (2004), derived from the pairwise Lennard-Jones potential, which may underestimate the energy corrugation (Zhang and Tadmor, 2017).

To determine $W_0(z)$ and $W_1(z)$, we compare the analytical function in Eq. (A5) with the numerical results by the DC method. For $z = 3.34$ Å, we obtain $W_0 = -38.8$ meV and $W_1 = -3.3$ meV by fitting the interaction energy at two in-plane locations, ($x = y = 0$) and ($x = \frac{a}{\sqrt{3}}$, $y = 0$). The resulting function by Eq. (A5) agrees closely with the numerical results shown in Fig. A1(b). Next, we determine the functions $W_0(z)$ and $W_1(z)$ based on the numerical results by the DC method at the two selected locations. The numerical results are fit closely with two analytical functions:

$$W_0(z) = \frac{a_0}{z^4} + \frac{b_0}{z^{10}}, \tag{A6}$$
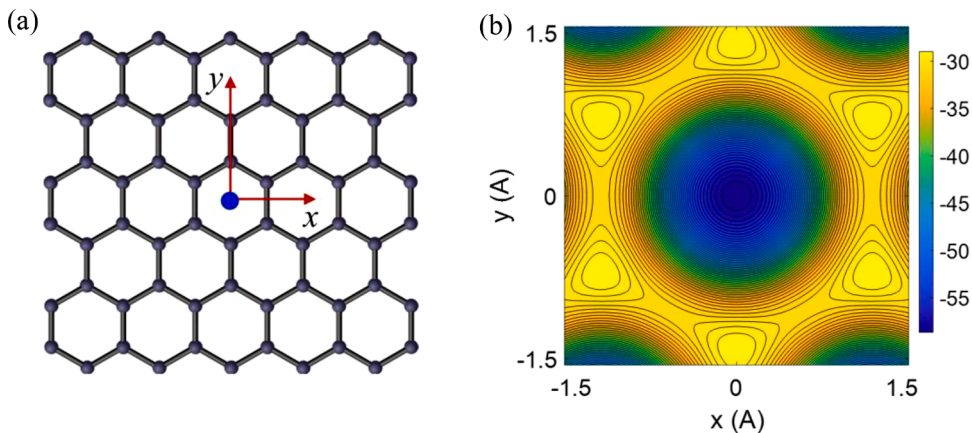
Fig. A1. (a) In-plane coordinate of a carbon atom on top of a graphene lattice; (b) Contours of the carbon-graphene interaction energy (in meV) calculated by the DC method with the KC potential at a constant normal separation ($z = 3.34$ Å).

$$W_1(z) = \frac{a_1}{z^4} + \frac{b_1}{z^{10}}, \tag{A7}$$

where $a_0 = -8.316$ eVÅ^4, $b_0 = 5402$ eVÅ^{10}, $a_1 = 0.01651$ eVÅ^4, and $b_1 = -658.1$ eVÅ^{10}.

The interaction energy between two graphene monolayers can be calculated directly using the KC potential or by the DC method (Zhang and Tadmor, 2017 and 2018). Alternatively, we can use the analytical function in Eq. (A5) for each atom-monolayer interaction. The interaction energy between a hexagonal ring of six carbon atoms and a monolayer is calculated by summation of six atom-monolayer interactions. As shown in Fig. A2, a periodic energy landscape is obtained with the hexagonal symmetry, similar to the interaction energy between one atom and the monolayer. However, the minimum energy is now obtained when the center of the hexagonal ring is located directly on top of a carbon atom in the graphene monolayer (i.e., AB stacking), and the maximum energy is obtained when it is located directly on top of the center of a hexagonal unit cell of graphene (i.e., AA stacking). Moreover, saddle points (SP) of the energy landscape are obtained when the center of the hexagonal ring is on top of the midpoint of a carbon-carbon bond in the graphene monolayer. To determine the interaction energy landscape between two graphene monolayers, the hexagonal ring is replicated periodically to yield a hexagonal lattice with the same interaction energy per atom. The interaction energy per unit area is then obtained by multiplying the number density (per unit area) of carbon atoms in one monolayer.

Similar to the atom-monolayer interaction, the monolayer-monolayer interaction energy (per unit area) can be fit approximately with an analytical function in form of (Kumar et al., 2015 and 2016)

$$U(x, y, z) = \rho_s W_0(z) - \rho_s W_1(z)\cos(G_1 y) - 2\rho_s W_1(z)\cos\left(\frac{G_1 y}{2}\right)\cos\left(\frac{\sqrt{3}G_1 x}{2}\right). \tag{A8}$$

Note that the coordinate (x, y, z) in Eq. (A8) is taken with the origin at the center of a hexagonal unit cell of graphene (one of the monolayers). Thus, the two graphene monolayers are in AA stacking if $x = y = 0$. A shift in the y direction leads to AB stacking (Fig. A2), with $x = 0$ and $y = -a$. Taking the AB stacking at the equilibrium separation ($z = z_0$) as the reference configuration, let (u_x, u_y, u_z) be the relative displacement between the two monolayers so that $x = u_x$, $y = -a + u_y$, and $z = z_0 + u_z$. Then, the interaction energy in Eq. (A8) can be re-written as a function of the relative displacements as

$$U(u_x, u_y, u_z) = U_0(u_z) + U_1(u_z)f(u_x, u_y). \tag{A9}$$

where

$$f(u_x, u_y) = \frac{3}{2} + \cos(G_1(u_y - a)) + 2\cos\left(\frac{G_1(u_y - a)}{2}\right)\cos\left(\frac{\sqrt{3}G_1 u_x}{2}\right), \tag{A10}$$

so that $f(0, 0) = 0$ and $U_0(u_z)$ represents the interaction energy of AB stacking. Comparing Eq. (A9) and Eq. (A8), we obtain

$$U_0(u_z) = \rho_s W_0(z_0 + u_z) + \frac{3}{2}\rho_s W_1(z_0 + u_z), \tag{A11}$$

$$U_1(u_z) = -\rho_s W_1(z_0 + u_z). \tag{A12}$$

With Eqs. (A6) and (A7), we obtain

$$U_0(u_z) = \rho_s \varepsilon_0 \left[-\frac{5}{3}\left(\frac{z_0}{z_0 + u_z}\right)^4 + \frac{2}{3}\left(\frac{z_0}{z_0 + u_z}\right)^{10} \right], \tag{A13}$$
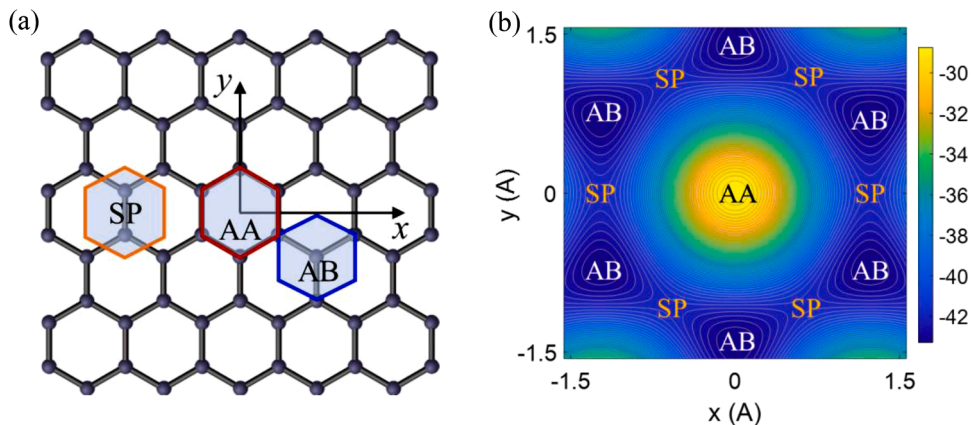
Fig. A2. (a) Stacking of a hexagonal ring of six atoms on top of a graphene lattice, illustrating the AA, AB and SP stacking orders. (b) Color contour of the monolayer-monolayer interaction energy (in meV per atom).

$$U_1(u_z) = \rho_s \varepsilon_1 \left[- \left(\frac{z_0}{z_0 + u_z} \right)^4 + \beta \left(\frac{z_0}{z_0 + u_z} \right)^{10} \right], \tag{A14}$$

where $\varepsilon_1 = a_1 z_0^{-4} = 0.133$ meV, $\beta = -\frac{b_1}{a_1} z_0^{-6} = 28.7$, and $\varepsilon_0 = 41.1$ meV.

Supplementary materials

Supplementary material associated with this article can be found, in the online version, at doi:10.1016/j.jmps.2021.104698.

References

Acik, M., Chabal, Y.J., 2011. Nature of graphene edges: a review. Jpn. J. Appl. Phys. 50, 070101.
Akinwande, D., Brennan, C.J., Bunch, J.S., Egberts, P., Felts, J.R., Gao, H., Huang, R., Kim, J.-S., Li, T., Li, Y., Liechti, K.M., Lu, N., Park, H.S., Reed, E.J., Wang, P., Yakobson, B.I., Zhang, T., Zhang, Y.-W., Zhou, Y., Zhu, Y., 2017. A review on mechanics and mechanical properties of 2D materials – graphene and beyond. Extreme Mech Lett 13, 42–77.
Alden, J.S., Tsen, A.W., Huang, P.Y., Hovden, R., Brown, L., Park, J., Muller, D.A., McEuen, P.L., 2013. Strain solitons and topological defects in bilayer graphene. Proc. Natl. Acad. Sci. 110, 11256–11260.
Braun, O.M., Kivshar, Y.S., 2004. The Frenkel-Kontorova Model: Concepts, Methods, and Applications. Springer Science & Business Media.
Dai, Z., Lu, N., Liechti, K.M., Huang, R., 2020. Mechanics at the interfaces of 2D materials: challenges and opportunities. Curr. Opin. Solid State Mater. Sci. 24, 100837.
Duong, D.L., Yun, S.J., Lee, Y.H., 2017. van der Waals layered materials: opportunities and challenges. ACS Nano 11, 11803–11830.
Gao, Y., 2010. A Peierls perspective on mechanisms of atomic friction. J. Mech. Phys. Solids 58, 2023–2032.
Geim, A.K., Grigorieva, I.V., 2015. Van der Waals heterostructures. Nature 499 (7459), 419–425.
Gigli, L., Manini, N., Benassi, A., Tosatti, E., Vanossi, A., Guerra, R., 2017. Graphene nanoribbons on gold: understanding superlubricity and edge effects. 2D Materials 4 (4), 45003.
Gigli, L., Manini, N., Tosatti, E., Guerra, R., Vanossi, A., 2018. Lifted graphene nanoribbons on gold: from smooth sliding to multiple stick-slip regimes. Nanoscale 10 (4), 2073–2080.
Gigli, L., Kawai, S., Guerra, R., Manini, N., Pawlak, R., Feng, X., Müllen, K., Ruffieux, P., Fasel, R., Tosatti, E., Meyer, E., Vanossi, A., 2019a. Detachment dynamics of graphene nanoribbons on gold. ACS Nano 13, 689–697.
Gigli, L., Vanossi, A., Tosatti, E., 2019b. Modeling nanoribbon peeling. Nanoscale 11 (37), 17396–17400.
Guo, Y., Guo, W., Cheng, C., 2007. Modifying atomic-scale friction between two graphene sheets: a molecular-force-field study. Phys. Rev. B 76, 155429.
Han, E., Yu, J., Annevelink, E., Son, J., Kang, D.A., Watanabe, K., Taniguchi, T., Ertekin, E., Huang, P.Y., van der Zande, A.M., 2020. Ultrasoft slip-mediated bending in few-layer graphene. Nat. Mater. 19, 305–309.
Jia, X., Hofmann, M., Meunier, V., Sumpter, B.G., Campos-Delgado, J., Romo-Herrera, J.M., Son, H., Hsieh, Y.-P., Reina, A., Kong, J., Terrones, M., Dresselhaus, M.S., 2009. Controlled formation of sharp zigzag and armchair edges in graphitic nanoribbons. Science 323, 1701–1705.
Jiang, L., Shi, Z., Zeng, B., Wang, S., Kang, J.-H., Joshi, T., Jin, C., Ju, L., Kim, J., Lyu, T., 2016. Soliton-dependent plasmon reflection at bilayer graphene domain walls. Nat. Mater. 15, 840–844.
Kawai, S., Benassi, A., Gnecco, E., Söde, H., Pawlak, R., Feng, X., Müllen, K., Passerone, D., Pignedoli, C.A., Ruffieux, P., 2016. Superlubricity of graphene nanoribbons on gold surfaces. Science 351 (6276), 957–961.
Kendall, K., 1975. Thin-film peeling - the elastic term. J. Phys. D: Appl. Phys. 8, 1449–1452.
Kim, S., Annevelink, E., Han, E., Yu, J., Huang, P.Y., Ertekin, E., van der Zande, A.M., 2020. Stochastic stress jumps due to soliton dynamics in two-dimensional van der Waals interfaces. Nano Lett 20, 1201–1207.
Kolmogorov, A.N., Crespi, V.H., 2005. Registry-dependent interlayer potential for graphitic systems. Phys. Rev. B 71, 235415.
Koren, E., Lortscher, E., Rawlings, C., Knoll, A.W., Duerig, U., 2015. Adhesion and friction in mesoscopic graphite contacts. Science 348, 679–683.
Kovalchick, C., Molinari, A., Ravichandran, G., 2014. Rate dependent adhesion energy and nonsteady peeling of inextensible tapes. J. Appl. Mech. 81, 041016.
Kumar, H., Dong, L., Shenoy, V.B., 2016. Limits of coherency and strain transfer in flexible 2D van der Waals heterostructures: formation of strain solitons and interlayer debonding. Sci. Rep. 6, 21516.
Kumar, H., Er, D., Dong, L., Li, J., Shenoy, V.B., 2015. Elastic deformations in 2D van der Waals heterostructures and their impact on optoelectronic properties: predictions from a multiscale computational approach. Sci. Rep. 5, 10872.
Liu, Y., Weiss, N.O., Duan, X., Cheng, H.-C., Huang, Y., Duan, X., 2016. Van der Waals heterostructures and devices. Nat. Rev. Mater. 1, 16042.
Lu, Q., Gao, W., Huang, R., 2011. Atomistic simulation and continuum modeling of graphene nanoribbons under uniaxial tension. Model. Simul. Mater. Sci. Eng. 19, 054006.
Lu, Q., Huang, R., 2010. Excess energy and deformation along free edges of graphene nanoribbons. Phys. Rev. B 81, 155410.
Mandelli, D., Leven, I., Hod, O., Urbakh, M., 2017. Sliding friction of graphene/hexagonal–boron nitride heterojunctions: a route to robust superlubricity. Sci. Rep. 7, 10851.
McGilly, L., Kerelsky, A., Finney, N., Shapovalov, K., Shih, E.-M., Ghiotto, A., Zeng, Y., Moore, S., Wu, W., Bai, Y., Watanabe, K., Taniguchi, T., Stengel, M., Zhou, L., Hone, J., Zhu, X., Basov, D.N., Dean, C., Dreyer, C.E., Pasupathy, A.N., 2020. Visualization of moiré superlattices. Nat. Nanotechnol. 15, 580–584.
Novoselov, K.S., Mishchenko, A., Carvalho, A., Castro Neto, A.H., 2016. 2D materials and van der Waals heterostructures. Science 353 (6298), aac9439.
Ouyang, W., Mandelli, D., Urbakh, M., Hod, O., 2018. Nanoserpents: graphene nanoribbon motion on two-dimensional hexagonal materials. Nano Lett. 18 (9), 6009–6016.
Pour, M.M., Lashkov, A., Radocea, A., Liu, X., Sun, T., Lipatov, A., Korlacki, R.A., Shekhirev, M., Aluru, N.R., Lyding, J.W., 2017. Laterally extended atomically precise graphene nanoribbons with improved electrical conductivity for efficient gas sensing. Nat Commun 8 (1), 1–9.
Rivlin, R.S., 1944. The effective work of adhesion. J. Paint Technol. 9, 215–218.
Ruffieux, P., Wang, S., Yang, B., Sánchez-Sánchez, C., Liu, J., Dienel, T., Talirz, L., Shinde, P., Pignedoli, C.A., Passerone, D., 2016. On-surface synthesis of graphene nanoribbons with zigzag edge topology. Nature 531 (7595), 489–492.
Sanchez, D.A., Dai, Z., Wang, P., Cantu-Chavez, A., Brennan, C.J., Huang, R., Lu, N., 2018. Mechanics of spontaneously formed nanoblisters trapped by transferred 2D crystals. PNAS 115 (31), 7884–7889.
Saraswat, V., Jacobberger, R.M., Arnold, M.S., 2021. Materials science challenges to graphene nanoribbon electronics. ACS Nano 15, 3674–3708.
Slota, M., Keerthi, A., Myers, W.K., Tretyakov, E., Baumgarten, M., Ardavan, A., Sadeghi, H., Lambert, C.J., Narita, A., Müllen, K., 2018. Magnetic edge states and coherent manipulation of graphene nanoribbons. Nature 557 (7707), 691–695.
Timoshenko, S., Woinowsky-Krieger, S., 1987. Theory of Plates and Shells, 2nd ed. McGraw-Hill, New York.
Tvergaard, V., Needleman, A., Lo, K.K., 1981. Flow localization in the plane strain tensile test. J. Mech. Phys. Solids 29, 115–142.

Verhoeven, G.S., Dienwiebel, M., Frenken, J.W., 2004. Model calculations of superlubricity of graphite. Phys. Rev. B 70 (16), 165418.

Wang, G., Dai, Z., Wang, Y., Tan, P., Liu, L., Xu, Z., Wei, Y., Huang, R., Zhang, Z., 2017. Measuring interlayer shear stress in bilayer graphene. Phys. Rev. Lett. 119, 036101.

Wang, G., Dai, Z., Xiao, J., Feng, S., Weng, C., Liu, L., Xu, Z., Huang, R., Zhang, Z., 2019. Bending of multilayer van der Waals materials. Phys. Rev. Lett. 123, 116101.

Yoo, H., Engelke, R., Carr, S., Fang, S., Zhang, K., Cazeaux, P., Sung, S.H., Hovden, R., Tsen, A.W., Taniguchi, T., Watanabe, K., Yi, G.C., Kim, M., Luskin, M., Tadmor, E.B., Kaxiras, E., Kim, P., 2019. Atomic and electronic reconstruction at the van der Waals interface in twisted bilayer graphene. Nat. Mater. 18, 448–453.

Zhang, K., Tadmor, E.B., 2017. Energy and moiré patterns in 2D bilayers in translation and rotation: a study using an efficient discrete–continuum interlayer potential. Extreme Mech. Lett. 14, 16–22.

Zhang, K., Tadmor, E.B., 2018. Structural and electron diffraction scaling of twisted graphene bilayers. J. Mech. Phys. Solids 112, 225–238.